Self-Centering and Energy Dissipation Behavior of Fe-SMA Prestressed Segmental Column Systems

Mohammad Esmaelian[a], Saim Raza[b], Masoud Motavalli[a,b], Moslem Shahverdi[a,b]*

[a] *School of Civil Engineering, University of Tehran, Tehran, 4563-11155, Iran*

[b] *Empa, Swiss Federal Laboratories for Materials Science and Technology, Dübendorf 8600, Switzerland*

*Corresponding author. Tel.: +41 58 765 4382, E-mail address: moslem.shahverdi@empa.ch

Abstract

Major seismic events can result in large residual displacements in conventional monolithic bridge columns, causing serviceability problems and expensive repair costs. In contrast, post-tensioned segmental columns exhibit excellent self-centering behavior and low residual drifts. However, such structures have limited energy dissipation capacity and require heavy mechanical equipment for prestressing using conventional tendons. This study proposes a novel self-centering segmental column system where prestressing is achieved by exploiting the unique shape memory effect (SME) characteristic of iron-based shape memory alloy (Fe-SMA) bars. A 3D finite element (FE) model was developed in ABAQUS and validated against the experimental results to evaluate the seismic performance of the proposed system. The model incorporated the experimentally validated material behavior of Fe-SMA bars under tension-compression reversals using the combined isotropic/kinematic hardening model. The validated model was used to conduct a parametric study to investigate the effect of five parameters, including total axial load ratio at constant post-tensioning force, relative contributions of post-tensioning force and gravity force to total axial load ratio, ratio of energy dissipating (ED) bars to Fe-SMA bars, confinement of concrete segments, and configuration of Fe-SMA bars, on the self-centering and energy dissipation behavior of the Fe-SMA prestressed segmental columns. The results showed that Fe-SMA bars are capable of providing both adequate self-centering and energy dissipation capacity to segmental columns owing to their self-prestressing and high ductility. The paper is concluded by evaluating the applicability of the existing self-centering criteria to Fe-SMA prestressed columns.

1 Introduction

Major seismic events pose a significant threat to the integrity and functionality of civil infrastructure such as bridge piers and building columns, necessitating the development of innovative structural systems capable of withstanding and recovering from earthquake-induced damage. Traditional reinforced concrete (RC) structures often exhibit irreversible deformations and residual displacements after seismic loading, resulting in costly repairs and prolonged downtime. The residual displacements refer to the permanent displacements that occur in the structure after the earthquake and can have serious implications for the structural integrity and operational functionality of structures. They can cause misalignment, cracking, and distortion of structural elements, compromising their load-bearing capacity and, more importantly, their serviceability. This is even more critical for bridge columns, where immediate serviceability after an earthquake is essential for emergency response, evacuation, and rescue. In the 1995 Kobe earthquake, more than one hundred RC bridge columns had residual drifts greater than 1.75%. Although these columns did not collapse, they had to be demolished because of misalignment with the superstructure [1]. The JRA (Japan Road Association) [2] classifies residual drift ratios greater than 1% as significant and recommends that the residual drift ratio for bridge piers should be maintained below 1% to ensure the repairability of bridge structures following a seismic event. Furthermore, several studies have proposed self-centering criteria to theoretically evaluate the self-centering ability of RC columns [3–8].

The ability of a column to recover residual drifts and return to its original position after experiencing inelastic deformations is called self-centering. This could be achieved by a combination of unbonded post-tensioning (PT) force and a moment-free connection at the foundation that allows for rocking behavior. Segmental columns with a discrete segment design at the foundation and along the column height, as well as the post-tensioning force, offer several advantages over conventional monolithic RC columns in

providing self-centering behavior after seismic events. The multiple discrete segment design results in controlled rocking of the segments under lateral loading without causing irreversible damage. The post-tensioning enhances the self-centering ability of segmental columns by providing a restoring force to help the column return to its original position. Accelerated construction, reduced environmental impact, and minimal traffic disruption are other advantages associated with precast segmental columns over conventional monolithic RC columns.

Numerous studies have been conducted to investigate various factors influencing the seismic performance of post-tensioned segmental columns [9–16]. Previous studies [5,17] have shown that the use of an unbonded prestressing system typically results in smaller residual drift compared to the bonded prestressing system, which results in large residual drifts and also increases the column strength and energy dissipation capacity through yielding of the prestressing reinforcement [15,18]. Another factor that may affect the seismic performance of precast segmental columns is the configuration of the prestressing reinforcement. According to the findings of Roh and Reinhorn [19], placing the tendons on each side of the column instead of the center results in an increase in lateral strength and eliminates the negative stiffness observed in the hysteretic curve. Nikbakht et al. [20] conducted a study to investigate the influence of strand position by comparing different arrangements of post-tensioned strands. The results showed that placing the strands closer to the circumference resulted in increased lateral strength, greater energy dissipation capacity, and higher residual drifts. However, all strands in this study were bonded to the surrounding concrete. Therefore, further research is needed to investigate the effect of the configuration of unbonded prestressing reinforcement on the seismic performance of segmental columns. The axial load ratio is another factor that plays a crucial role in the seismic performance of precast segmental columns. This ratio consists of two components, the prestressing force and the gravity load of the superstructure. The presence of a vertical gravity load causes a P-Δ effect when the column is deformed. However, this effect is not observed with the prestressing force acting perpendicular to the column. To ensure adequate ductility, several studies suggest a threshold of 20% for the total axial load ratio [9,21,22]. Additional research is required to investigate the individual contributions of each component of the axial load ratio to the seismic performance of segmental columns.

Despite the excellent self-centering behavior and notable advantages of precast segmental columns, the use of these structures is still limited to areas with lower seismic activity due to their low energy dissipation capacity. To address this issue, researchers have explored several strategies that incorporate internal ED bars [5,11,12,14,15] or external ED devices [10,19,23,24]. In addition, the application of new structural materials such as fiber reinforced steel concrete (SFRC) [28,29], engineered cementitious composites (ECC) [30,31], hybrid fiber-reinforced concrete (HyFRC) [29], ultra-high-performance fiber-reinforced concrete (UHPFRC) [30], and steel or FRP jacket [9,10,31] have been considered in the plastic hinge region (i.e the bottom segment) of these columns. Ou et al. [32] proposed a precast segmental column design using cast-in-place (CIP) construction for the lower portion, which resulted in remarkable ductility and energy dissipation [32–35]. The concept of hybrid sliding-rocking (HSR) bridge columns was introduced by Sideris [36] and Sideris et al. [13,37]. These HSR columns are precast concrete segmental columns that incorporate internal unbonded post-tensioning, rocking joints at the column ends, and intermediate sliding (HSR) joints along the column height. The HSR columns incorporate additional energy dissipation through the use of low-friction materials that allow friction at the slip joints. Any residual sliding that may occur is typically minimal and can be eliminated by hydraulic or mechanical means [38,39]. Another limitation in relation to post-tensioning segmental columns with conventional tendons

is that the post-tensioning process requires the installation of heavy mechanical equipment, including hydraulic jacks, anchor heads, and end anchorages, which is cumbersome.

A possible solution to overcome the above-mentioned two limitations could be to use iron-based shape memory alloys (Fe-SMAs), as a prestressing reinforcement in segmental columns. Fe-SMA belongs to a class of smart materials that show unique pre-stressing characteristics upon heating through a phenomenon known as shape memory effect [40]. The shape memory effect refers to the unique property by which Fe-SMA can recover inelastic deformations upon thermal activation. To activate Fe-SMA bars, the bars are first prestrained to a target strain and then unloaded. The prestrained bars are then clamped at both ends and heated to a target temperature of 160^{o} C or higher. The clamping prevents bars to recover inelastic deformation, resulting in a prestress called recovery stress [41–43]. Fe-SMA bars are easy to install and work with, as the thermal activation can be simply done by electrical resistive heating or gas flame heating without any need for the installation of heavy mechanical equipment [41,43]. Fe-SMA bars are also expected to increase the energy dissipation capacity of segmental columns compared to conventional tendons due to their lower yield strength and their ability to contribute to the energy dissipation capacity after yielding during cyclic loading owing to their high ductility . These properties make Fe-SMAs an attractive alternative for prestressing RC structures, not only for strengthening but also for the design of new structures. The application of prestressed Fe-SMA for self-centering of existing bridge columns has recently been explored in [44]. The use of Fe-SMA in civil engineering for flexural and shear strengthening purposes of beams, slabs, and masonry structures has received considerable attention in recent years [40–42], [45–65]. However, the application of Fe-SMA for the design of new smart structures, such as Fe-SMA prestressed self-centering segmental columns and walls, has been limited thus far. This was mainly because the cyclic behavior of activated Fe-SMA was not well understood. Recently, however, the cyclic and fatigue behavior of activated and non-activated Fe-SMA has been experimentally investigated [66–69]. This provides a promising opportunity to explore the use of activated Fe-SMA bars for novel self-centering applications for segmental columns under extreme loading events involving cyclic tension-compression reversals.

This study proposes a novel self-centering segmental column system, where prestressing is achieved by exploiting the unique characteristics of Fe-SMA bars. To evaluate the seismic performance of the proposed system, a 3D finite element (FE) model is developed in ABAQUS and validated against the experimental results. The model incorporates the material behavior of Fe-SMA bars under tension-compression reversals using the combined isotropic/kinematic hardening model. The material model is calibrated against the experimental behavior of Fe-SMA under cyclic reversals. The validated model is used to conduct a parametric study to investigate the effect of various parameters including total axial load ratio at constant PT force, relative contributions of PT force and gravity force to total axial load ratio, ratio of ED bars to Fe-SMA bars, confinement of concrete segments, and configuration of Fe-SMA bars on the self-centering and energy dissipation behavior of the Fe-SMA prestressed segmental columns. The paper is concluded by evaluating the applicability of the existing self-centering criteria to Fe-SMA prestressed columns.

2 Finite Element Modelling

2.1 Proposed Segmental Column System

The segmental column system proposed in this study utilizes the novel Fe-SMA bars as the prestressing reinforcement. The reference column has an aspect ratio of six and consists of four 610 mm diameter

precast concrete segments. The base segment has a height of 610 mm and the upper segments are 900 mm high. The segments are reinforced with 8⌀12.7 evenly spaced steel longitudinal bars which are discontinuous at the segment joints. Each segment is confined with 9.5 mm stirrups spaced at 75 mm, resulting in a transverse reinforcement ratio (by area) of 0.31%. 14⌀18 unbonded Fe-SMA bars are used for prestressing the column. These bars are evenly distributed around the column perimeter, resulting in a longitudinal reinforcement ratio of 1.22%. The Fe-SMA bars are bonded in the foundation and top loading block and left unbonded along the column height to reduce strain concentration and early loss of prestress. The recovery stress of each Fe-SMA bar is 300 MPa, which resulted in a total PT load ratio of 7.5% in the column. The design axial load ratio due to gravity was 12.5%, resulting in a total axial load ratio of 20% on the column, which is typical for bridge columns [9,21,22]. Figure 1 shows the design details of the proposed system.

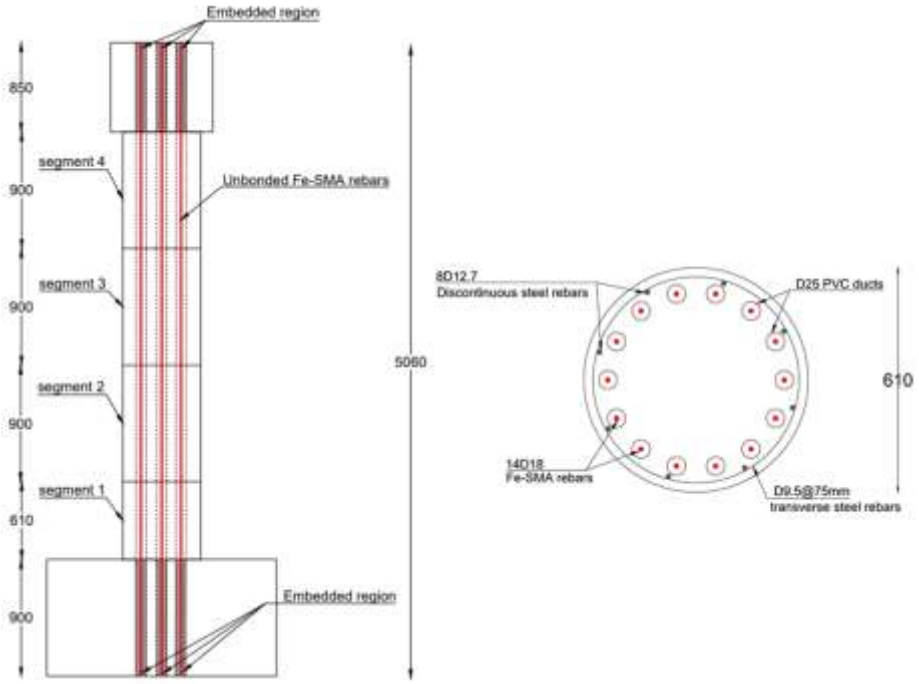

Figure 1 Design details of the proposed system (S1)

2.2 Material modeling

2.2.1 Concrete

Concrete damage plasticity (CDP) is utilized in this study to model the inelastic behavior of concrete. Smeared crack model, brittle cracking model, and the concrete damage plasticity (CDP) models are available in ABAQUS for modelling the material behavior of concrete [70]. The smeared crack model is typically employed when concrete is subjected to monotonic loadings. The brittle cracking model is accurate for modeling brittle materials such as brittle rocks or unreinforced concrete since it considers a linear elastic behavior in compression. The concrete damaged plasticity (CDP) model is primarily meant to offer a general capacity for the analysis of RC structures subjected to monotonic, cyclic and/or dynamic loadings [70]. Since the columns considered in this study are RC structures subject to cyclic loadings, the concrete damaged plasticity (CDP) model is utilized to model the inelastic behavior of concrete.

The concrete damage plasticity (CDP) model is defined based on five plasticity parameters and uniaxial material behavior in tension and compression. The behavior of the material under cyclic loading is characterized by implementing damage data in tension and compression. The damage data defines the stiffness degradation of the material subjected to repeated cycles. Table 1 summarizes the material properties of concrete and Table 2 provides the values of plasticity parameters used as input for the concrete damage plasticity (CDP) model.

The stress-strain relationships proposed by Mander et al. [71] are utilized in this study to model the compressive behavior of unconfined and confined concrete with spirals and steel jacket. In Mander's model, the spacing of the spirals, the jacket thickness, and the resulting confining pressure influence the ultimate strength and softening behavior of the concrete after the peak stress. Equation 1 gives the stress-strain relationship of the Mander model where f'_{cc} is the confined concrete strength obtained from equation 2, ε_{cc} is the corresponding strain, E_c is the tangent modulus of elasticity, E_{sec} is the secant modulus defined as $E_{sec} = \frac{f'_{cc}}{\varepsilon_{cc}}$. In equation **Error! Reference source not found.**, f'_l is the confining pressure resulting from the jacket or spirals, f'_{co} is the unconfined concrete strength. The Mander model sets the value of confined concrete strength (f'_{cc}) equal to the unconfined concrete strength (f'_{co}) to simulate the behavior of unconfined concrete. Further details of the Mander model can be found in [71].

$$f_c = \frac{f'_{cc} E_c \varepsilon_c / \varepsilon_{cc}}{E_{sec} + (E_c - E_{sec})(\varepsilon_c / \varepsilon_{cc})^{E_c/(E_c - E_{sec})}} \quad 1$$

$$f'_{cc} = f'_{co}\left(-1.254 + 2.254\sqrt{1 + \frac{7.94 f'_l}{f'_{co}}} - 2\frac{f'_l}{f'_{co}}\right) \quad 2$$

Figure 2(a) shows the stress-strain curves of unconfined and confined concrete with stirrups and steel jacket based on the models described earlier. Figure 2(b) shows the effect of different stirrup spacings on the stress-strain curve of concrete, where reduced stirrup spacing improve the softening behavior and peak stress significantly.

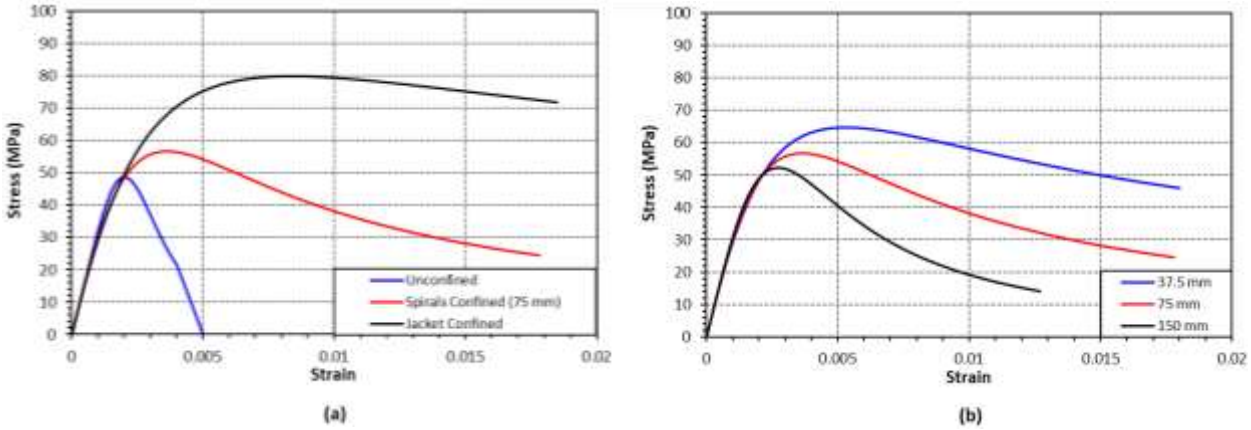

Figure 2 Stress-strain curves of (a) unconfined and confined concrete (b) confined concrete with different spiral spacings

In tension, a linear-elastic behavior is assumed for concrete prior to peak tensile strength. The stress-crack opening method is used in this study to define the post-peak response in tension to avoid unnecessary convergence problems. The exponential function proposed by Cornelissen et al. [72] is given as input to the CDP model for defining the tensile behavior (equation 3).

$$\frac{\sigma}{f_t} = f(\omega) - \frac{\omega}{\omega_c} f(\omega_c)$$
$$f(\omega) = \left[1 + \left(\frac{c_1 \omega}{\omega_c}\right)^3\right] \exp\left(-\frac{c_2 \omega}{\omega_c}\right)$$
$$\omega_c = 5.14 \frac{G_f}{f_t} \quad (3)$$

Where, ω is the crack-opening displacement, $f(\omega)$ is a displacement function, ω_c is the crack-opening displacement at which stresses can no longer be transferred, G_f is the fracture energy of concrete, and c_1 and c_2 are material constants with values of 3 and 6.93 for normal-density concrete, respectively. The fracture energy (G_f) is derived from CEB-FIB [73] (equation 4), and the concrete tensile strength according to Table 1 is 4.1 MPa. The post-peak tensile behavior of concrete is shown in Figure 3.

$$G_f = (0.0469 {d_a}^2 - 0.5 d_a + 26)\left(\frac{f_c'}{10}\right)^{0.7} \quad (4)$$

As mentioned earlier, the CDP model incorporates damage data to account for the stiffness degradation of the concrete under cyclic loadings. According to [74], the compressive damage parameter (d_c) is defined as follows:

$$d_c = 1 - \frac{\sigma_c E_c^{-1}}{\varepsilon_c^{pl}(1/b_c - 1) + \sigma_c E_c^{-1}} \quad (5)$$

Where ε_c^{pl} is the plastic compressive strain, σ_c is the compressive stress, E_c is the elastic modulus, and b_c is recommended to be 0.7. The tensile damage parameter (d_t) is developed by Pavlovic et al. [75] as follows:

$$d_t = 1 - \frac{\sigma_t}{\sigma_{t0}} \quad (6)$$

Where σ_t is the tensile stress and σ_{t0} is the concrete tensile strength.

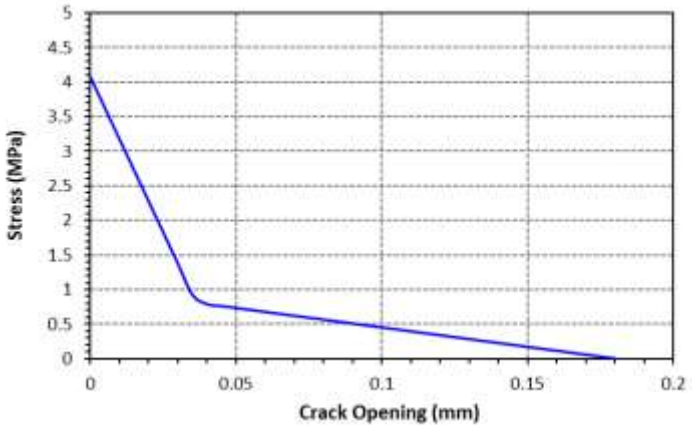

Figure 3 Tensile behavior of concrete

Table 1 Material properties of concrete

Mechanical Property	*Value*
Compressive strength (MPa)	48.7
Tensile strength (MPa)	4.1
Elastic modulus (GPa)	32.8
Poisson's ratio	0.2

Table 2 Input parameters of CDP model in ABAQUS

Parameter	*Value*
Dilation angle, $\boldsymbol{\psi}$ *(°)*	40
Plastic potential eccentricity, $\boldsymbol{e}$	0.1
Stress ratio, $\boldsymbol{\sigma_{b0}/\sigma_{c0}}$	1.16
Shape of the yielding surface, $\boldsymbol{K_c}$	0.6667
Viscosity parameter, $\boldsymbol{\mu}$	0.0001

2.2.2 Steel reinforcement

All steel reinforcement, including longitudinal and transverse bars, ED bars, steel tendons, and steel jackets, are defined using the elastic-perfectly plastic stress-strain material model with the isotropic plasticity. Mechanical properties of the steel reinforcement used in this study are listed in Table 3.

Table 3 Material properties of steel reinforcement

Materials	*Mechanical Property*	*Value*
Longitudinal,Transverse, and ED Bars	Elastic modulus (GPa)	206
	Yield strength (MPa)	443
	Poisson's ratio	0.3
Steel Jacket	Elastic modulus (GPa)	206
	Yield strength (MPa)	303
	Poisson's ratio	0.3
Activated Fe-SMA	Elastic modulus (GPa)	151

Non-Activated Fe-SMA	Poisson's ratio	0.25
	Yield strength (MPa)	439
	Ultimate strength (MPa)	800
	Failure strain (%)	>30
	Elastic modulus (avg) (GPa)	195
	Poisson's ratio	0.25
	Yield strength (MPa)	400
	Ultimate strength (MPa)	800
	Failure strain (%)	>30

2.2.3 Iron-based shape memory alloy

The material behavior of activated and non-activated Fe-SMA under tension-compression reversals was modeled using the combined isotropic/kinematic hardening model. The developed model was calibrated with the results of experimental cyclic tests conducted by Raza et al. [69]. Moreover, the present study conducted another cyclic test as part of the same experimental campaign on a non-activated Fe-SMA specimen (denoted as SP 1). Geometric details and loading protocols of the experimental specimens are summarized in Table 4.

Table 4 characteristics of Fe-SMA specimens

Specimen	*Loading*	*State*	*Protocol*
SP 1	Cyclic	Non-activated	Incremental amplitudes (0.03%, 0.06%, 0.12%, 0.25%, 0.5%, 1.0%)
SP 10 [69]	Cyclic	Activated @ 160 °C	Incremental amplitudes (0.1%, 0.2%, 0.3%, 0.4%, 0.5%, 0.6%, 0.7%, 0.8%, 0.9%, 1.0%)
SP 12 [69]	Cyclic	Non-activated	Incremental amplitudes (0.5%, 1.0%, 1.5%, 2.0%, 2.5%, 3.5%, 4.0%, 4.5%, 5.0%) Specimen L/D = 3

The combined isotropic/kinematic hardening model is based on the theory proposed by Chaboche [76] and consists of two kinematic and isotropic components, which refer to the translation and uniform expansion of the yield surface in stress space, respectively. The translation of the yield surface in the stress space (Bauschinger effect) is defined by the back stress (Equation 7). According to the ABAQUS documentation, several backstress components can be included to effectively improve the modeling results [70]. Each backstress component is a function of $C_k$and γ_k where C_k is the kinematic hardening modulus and γ_k is the decreasing rate of C_k with respect to increasing plastic deformation (ε^p). The kinematic hardening of the material is determined by calibrating the values of C_k and γ_k. There are three methods to define kinematic hardening in ABAQUS: 1) Direct parameters 2) Stabilized cycle 3) Half cycle.

$$\alpha = \Sigma_{k=1}^{n} \frac{C_k}{\gamma_k}\left(1 - e^{-\gamma_k \varepsilon^p}\right) \quad 7$$

The stabilized cycle method is used in this study to calibrate the kinematic hardening model according to the procedure defined in [70]. The data pairs of (σ_i, $\varepsilon_i^{\mathrm{pl}}$) derived from the stabilized cycle are given to ABAQUS as input, and ABAQUS automatically determines the kinematic parameters and reports them in

the data file when model definition data are requested [70]. The input data pairs of (σ_i, $\varepsilon_{\mathrm{i}}^{\mathrm{pl}}$) are obtained from the stabilized stress-strain curve by subtracting the elastic strain and shifting the strain axis to $\varepsilon_{\mathrm{p}}^{0}$ as described below:

$$\varepsilon_{\mathrm{i}}^{\mathrm{pl}} = \varepsilon_{\mathrm{i}} - \frac{\sigma_{\mathrm{i}}}{E} - \varepsilon_{\mathrm{p}}^{0} \quad 8$$

The first data pair is therefore implemented as (σ_1, 0.0). In Equation 8, $\varepsilon_{\mathrm{p}}^{0}$ represents the minimum plastic strain at zero stress as shown in Figure 4. For each data pair, the values of α_i are obtained from:

$$\alpha_i = \sigma_i - \frac{\sigma_1 + \sigma_n}{2} \quad 9$$

Where σ_1 and σ_n are the stress values in the first and last data pair, respectively. With the obtained data pairs (α_i, $\varepsilon_{\mathrm{i}}^{\mathrm{pl}}$) and using equation 7, ABAQUS determines the kinematic hardening parameters (C_k and γ_k) [70]. It is worth noting that in the combined hardening model, the tensile/compressive unloading slope is equal to the Young's modulus (Figure 4), so the Young's modulus defined in ABAQUS must be calculated based on the unloading slope where the load direction changes from tension/compression to compression/tension. The values of Young's modulus used in this study to model the cyclic behavior of activated and non-activated Fe-SMA are summarized in Table 3. According to the elastic modulus values in Table 3, the activated and non-activated Fe-SMA have an elastic modulus of 151 and 195 GPa, respectively. It should be noted that the reported Young's modulus of the non-activated Fe-SMA in this study belongs to SP 1, which was calculated using measurements from the extensometer. The Young's modulus from the experimental stress-strain curve of SP 12 was found to be lower and in the range of 75-85 GPa because its strains were determined from machine displacement data (without any post-processing) as extensometer was not used in the test of this specimen. Despite the different modulus values, the results of the two specimens are compared to show the robustness of this approach in capturing the stress-strain behavior of the material, where it is important to have the correct unloading slope as an input to the model.

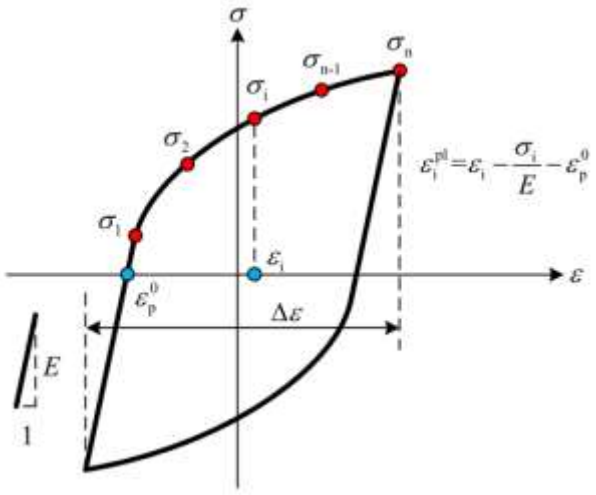

Figure 4 Stress-strain curve of stabilized cycle for calibration of kinematic hardening parameters (Reprinted from [77]*)*

To verify the accuracy of the calibrated material model against experimental data, a unit-cubic model was developed and subjected to the same loading protocols as the tested specimens. The unit cubic finite element model consists of a single C3D8R element with unit dimensions. The reason for choosing the unit cubic model is to reduce the computational cost and to prevent the occurrence of necking and premature rupture of the specimen. The unit cubic model is fully constrained on the bottom face to simulate the fixed boundary condition, and the applied strain is implemented on the top face as a displacement control load according to the loading protocols in Table 4. The lateral degrees of freedom are free to allow the Poisson phenomenon in the specimen. In the case of activated Fe-SMA, the prestressing force is applied to the entire element through the Predefined Field panel. The static-general analysis type with consideration of nonlinear effects of large deformations is used to perform the cyclic analyses.

Figure 5 compares the results of the combined hardening model with the experimental results of non-activated Fe-SMA bars. The results indicate that the combined hardening model can reasonably predict the cyclic behavior of non-activated Fe-SMA in terms of peak stress and tensile/compressive unloading shape of the curve (Figure 5). However, the slight difference that occurs in the tensile/compressive unloading part is due to the limitation of the combined hardening model in capturing the pseudoelastic behavior of Fe-SMA. Furthermore, local buckling of the specimens is responsible for the discrepancy in peak compressive stresses at high strain amplitudes. Comparison of the results of the combined hardening model with the experimental results for activated Fe-SMA in Figure 6 shows that the model is able to reasonably capture the tensile behavior, but overestimates the compressive stresses. This is because unlike non-activated Fe-SMA, the activated Fe-SMA exhibits asymmetric cyclic behavior due to the pre-straining performed before activation. As a result, it can be seen in the experimental curve shown in Figure 6 that while the maximum tensile stress is about 550 MPa, the maximum compressive stress is only about 380 MPa. The discrepancy in the experimental and modelling results is because the combined kinematic/isotropic model is only capable of capturing symmetrical cyclic behavior.

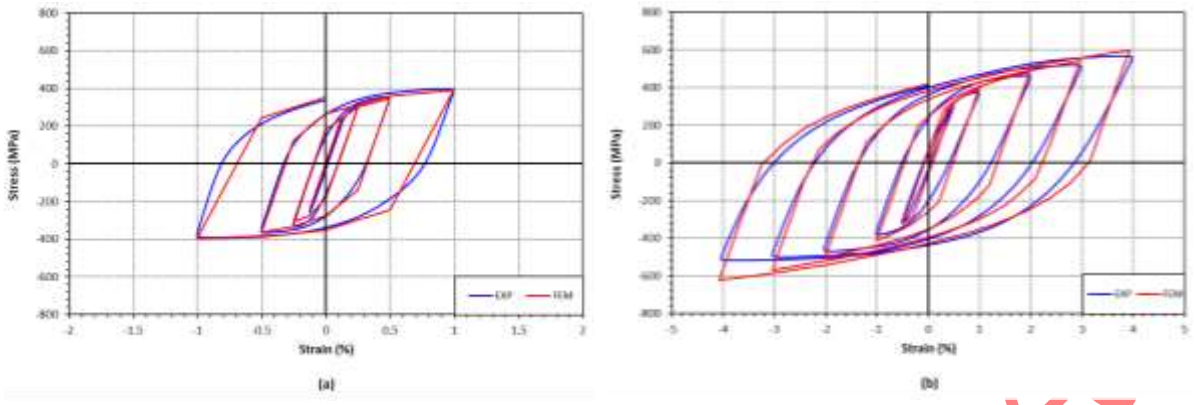

Figure 5 Results of material modeling of non-activated Fe-SMA (a) SP 1 (b) SP 14

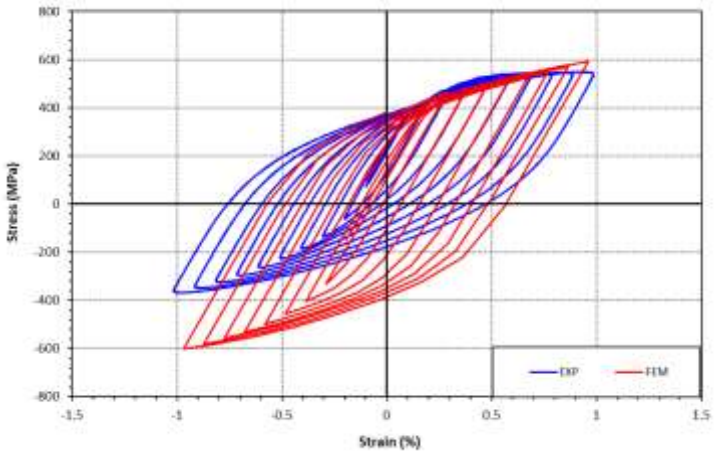

Figure 6 Results of material modeling of activated Fe-SMA (SP 10)

Table 5 Calibrated material model parameters

Specimens	$\sigma\|_0$	C_1	γ_1	C_2	γ_2
SP 1 – 1%	268.96	132521	29078	33763	268.81
SP 10 – 1%	340	41704	142	156750	2574
SP 12 – 4%	301.6	8050.4	20.9	19532	228.6

Despite the limitation of the combined/hardening model in accurately capturing the compressive stresses of activated Fe-SMA, the modelling approach is deemed appropriate for modelling the behavior of activated Fe-SMA bars in the proposed segmental columns. This is because the Fe-SMA bars used in the columns are prestressed and therefore small compressive stresses are expected in the bars under cyclic loading. In addition, the bars are unbonded, which means that the majority of the compression will be carried by the concrete, resulting in minimal compressive strains in the bars, as shown later in Section 3.3.5. The material model parameters calibrated for each specimen are summarized in Table 5. The proposed parameters are only valid in the strain ranges for which they have been calibrated. Additional strain ranges require new experimental data and further calibration.

2.3 Column Model description

Figure 8 shows the finite element model of the proposed segmental column. All concrete components, including precast segments, loading block, and foundation, were modeled using eight-node linear 3D brick reduced integration elements (C3D8R). All the steel reinforcements, including longitudinal and transverse bars, ED bars, as well as Fe-SMA bars, were modeled with two-node linear truss elements (T3D2) that provide only axial stiffness.

2.3.1 Interactions and constraints

The surface-to-surface contact has been used to define the interaction between the column segments. Contact behavior at the joints consists of two components 1) Tangential behavior and 2) Normal behavior. The tangential contact behavior between the master and slave surfaces is modeled by tangential friction. The coefficient of friction between the segments is assumed to be 0.5 based on the recommendations of [78]. The normal contact behavior is modeled by hard contact, which enables the surfaces to separate without resistance and to develop compression when the surfaces come into contact.

ED bars and discontinuous steel reinforcement were fully embedded in the surrounding concrete using the "embedded region" constraint in ABAQUS to simulate the interaction between reinforcement and concrete. Fe-SMA bars were embedded with a similar constraint only at the foundation and the loading block, leaving the remaining length unbonded.

2.3.2 Loading and boundary conditions

All degrees of freedom of the column foundation are constrained to simulate the rigid boundary condition resulting in a cantilever column configuration. The prestressing force is defined using the Predefined Field, Initial Stress option in ABAQUS in the first loading step. The first step allows the model to reach equilibrium under the initial prestressing force. The axial load is then applied to the top surface of the loading block as a surface pressure load. Finally, the loading block is subjected to a displacement controlled cyclic lateral loading according to the loading protocol shown in Figure 7.

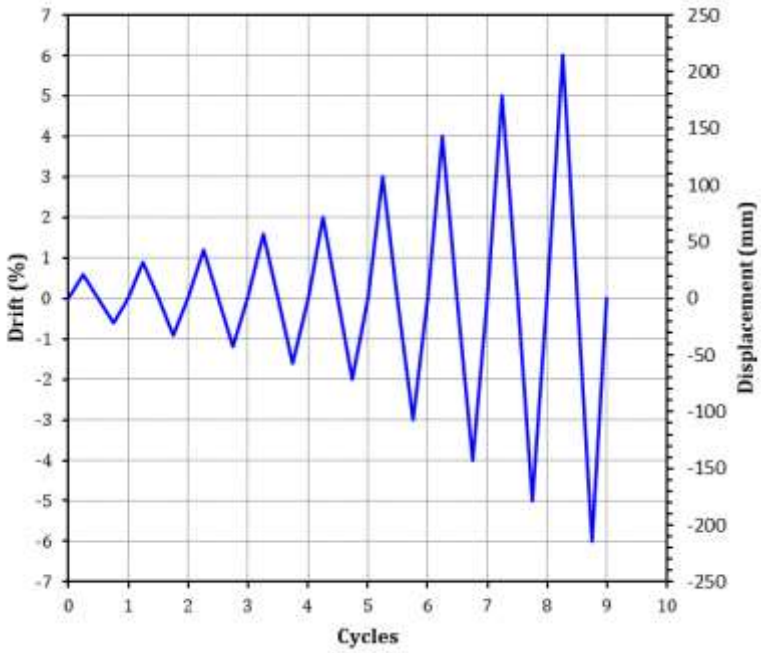

Figure 7 Loading protocol of the applied lateral drift ratio

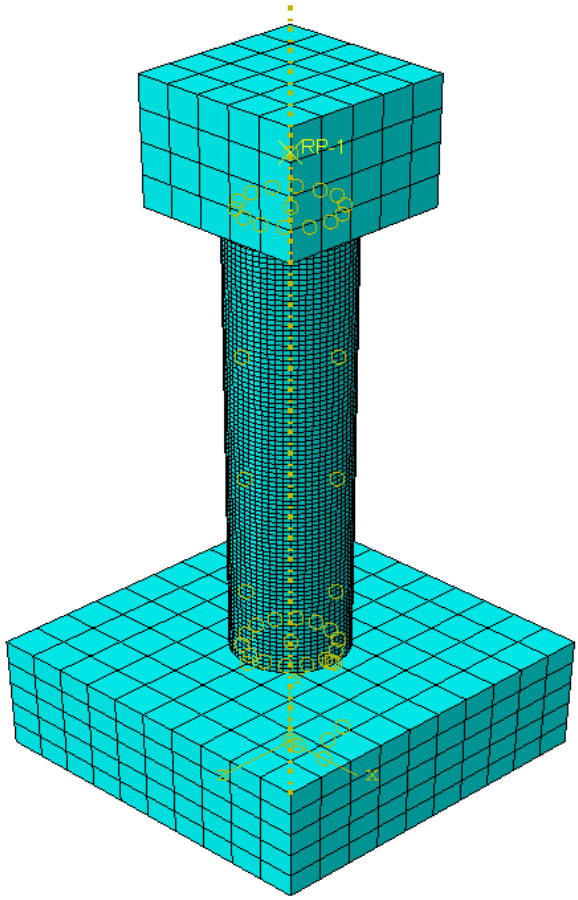

Figure 8 General view of segmental column prestressed by activated Fe-SMA bars

3 Results and Discussion

3.1 Validation of the Finite Element Model

The finite element model of the segmental column was validated by comparing against the experimental results of Hewes and Priestley [9]. The tested column (JH1) in [9] was a segmental column prestressed by a central steel tendon and confined by a 6 mm steel jacket around the bottom segment. The tendon was left unbonded in a 140 mm diameter duct across the height of the column. Figure 9 shows the design details of JH1. The tendon with an area of 2665 mm^2 was post-tensioned to 1009 MPa, resulting in an axial load of 2689 KN, corresponding to a PT load ratio of 19.9 %. Truss elements (T3D2) were used to model the tendon and were embedded in the surrounding concrete at the ends of the tendon to simulate anchorage. Surface-to-surface contact elements with tangential behavior were utilized to simulate the contact between the tendon and the duct, assuming a coefficient of friction of zero. The steel jacket was modeled using Shell elements (S4R). A similar contact behavior as column joints was employed to simulate the contact between the steel jacket and the bottom segment. The gravity load was 890 KN, resulting in a gravity load ratio of 6.6%, leading to a total axial load ratio of 26.5%. The cyclic lateral displacement loading was applied to the top loading block up to 3% drift following the loading protocol in Figure 7. The results were validated in terms of the global and local behavior of the specimen. The adopted mesh size was selected based on a sensitivity analysis to ensure a balance between computational cost and output accuracy. The sensitivity analysis was performed with respect to the hysteretic force-displacement response and damage pattern of the model. A mesh size of 45 mm was used for the steel jacket and concrete segments. Mesh sizes of 160 and 90 mm were used for the tendon and discontinuous steel reinforcement, respectively.

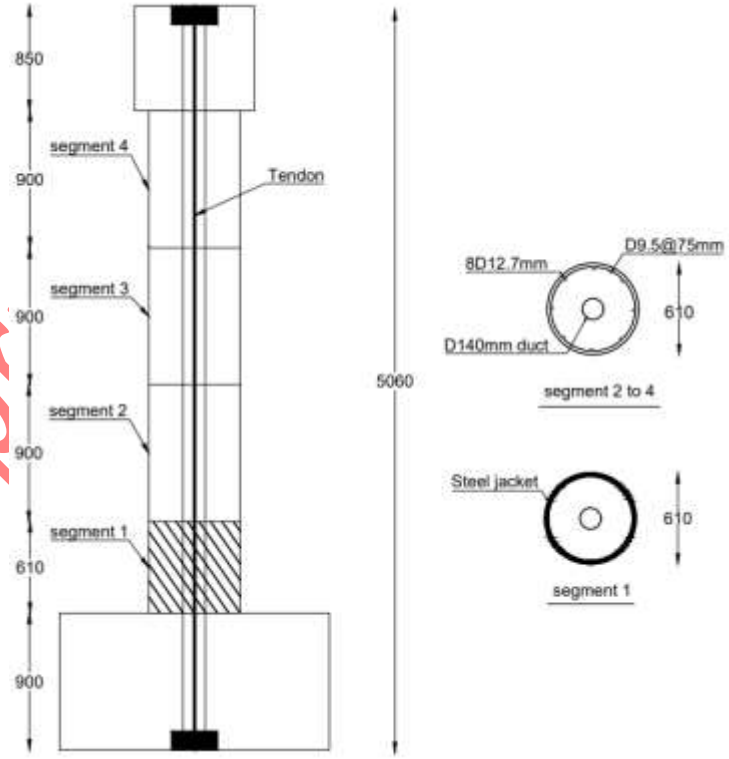

Figure 9 Design details of the specimen (JH1) used for validation of FE model (Reproduced from [9]*)*

3.1.1 Global behavior

The hysteretic lateral force-displacement behavior of the specimen was used to validate the global behavior of the column predicted by the finite element model. The comparison of the experimental and numerical hysteretic curves is shown in Figure 10. The model was able to reasonably predict the experimental results in terms of peak forces and stiffness degradation at high drift ratios. The experimental and numerical peak lateral force and the corresponding error in the lateral force at each drift ratio are presented in Table 6. The results indicate that the error in predicted lateral force in the negative direction is slightly larger than in the positive direction. This difference is mainly due to the asymmetric experimental hysteretic behavior in the positive and negative loading directions. The maximum error in the prediction of lateral force in the positive and negative directions was 10.0 % and 15.6 %, respectively, which is quite reasonable.

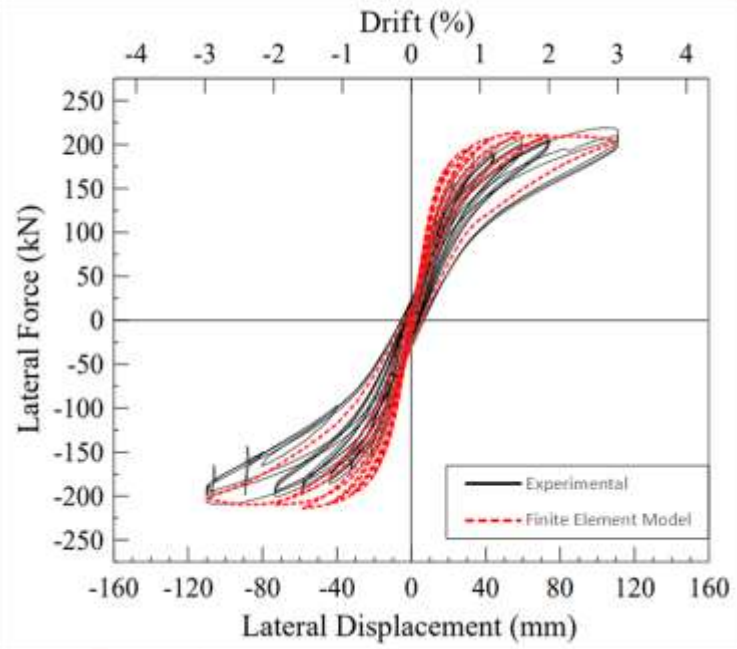

Figure 10 Comparison of experimental and numerical lateral load-displacement hysteretic response

Table 6 Comparison of experimental and numerical peak lateral forces at each drift ratio

Drift ratio (%)	*Experimental (KN)*	*Numerical (KN)*	*Error (%)*
0.6	164.7	181.2	10.0
-0.6	-156.2	-180.6	15.6
0.9	186.7	197.7	5.9
-0.9	-175.6	-199.9	13.8
1.2	196.9	207.7	5.5
-1.2	-185.3	-209.6	13.1
1.6	206.1	213.7	3.7
-1.6	-194.9	-214.8	10.2
2	210.4	210.4	0.0
-2	-199.4	-210.7	5.7
3	217	202.9	6.5
-3	-206.3	-203.4	1.4

3.1.2 Local behavior

To validate the local behavior, the damage patterns of the model are compared with the experimentally observed damage patterns. Figure 11 compares the distribution of damage patterns in the modelled column with the experimental results at 3% drift ratio. The black area in the second segment in Figure 11(c) represents concrete elements with strains exceeding the strain at the peak stress of unconfined concrete, indicating spalling of the concrete cover in the model. The same damage pattern could be observed in the tested column where concrete in segment 2 spalled at 3% drift ratio as shown in Figure 11(a). In addition, the experimental results show concrete crushing at the very bottom of the first segment as shown in Figure 11(b). This occurred because the steel jacket was placed 25 mm above the foundation surface to avoid contact between the jacket and the foundation during the test. The numerical model was also successful in capturing this damage as highlighted in Figure 11(c). The validation of the experimental results in terms of global and local behavior indicates that the model can reasonably predict the cyclic behavior of prestressed segmental columns. In the next section, the validated modelling approach is used to study the effect of different design parameters on the cyclic behavior of precast segmental columns prestressed with Fe-SMA bars.

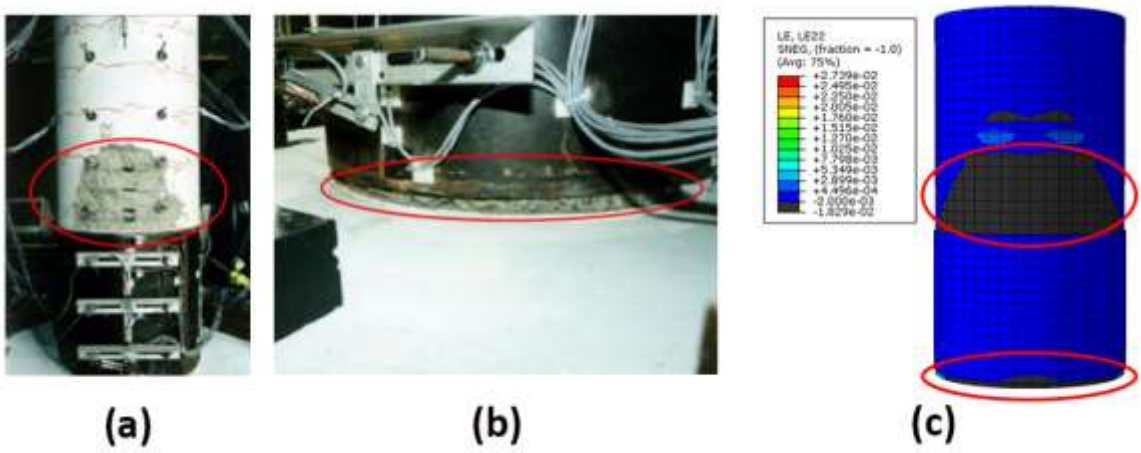

Figure 11 Comparison of damage pattern: (a) Spalling of concrete in the second segment (JH1) [9] (b) Concrete crushing at the bottom part of segment one (JH1) [9] (c) Compressive axial strains in numerical model at 3% drift ratio

3.2 Mesh sensitivity analysis

As the main focus of the current study is to investigate the self-centering behavior of segmental columns prestressed with Fe-SMA bars, a separate mesh sensitivity analysis was performed on the specimens of the parametric study to ensure that the results of residual drifts are not affected by the mesh size. Two specimens, one with and one without ED bars, were used in the sensitivity analysis. The reason for choosing the specimen without ED bars is that due to the absence of ED reinforcement, the concrete may suffer more severe damages and thus the mesh size can play a more important role in the column behavior. Therefore, a wider range of mesh sizes was used in the mesh sensitivity analysis of this specimen to account for this concern. Furthermore, the specimen with ED bars was included in the sensitivity analysis to examine the effect of mesh size on column behavior in the presence of ED reinforcement.

Four different mesh sizes for concrete elements (i.e. 45, 40, 35, and 30 mm) were considered for specimen consisting of ED bars. For the specimen without ED bars, two different mesh sizes were considered for concrete elements (i.e. 45 and 35 mm) and two for ED bars (i.e. 60 and 30 mm). Since the Fe-SMA bars in both specimens were unbonded, the mesh size had little impact on the results. Therefore, a 280 mm mesh size was used for the Fe-SMA bars in both specimens. The results of the mesh sensitivity analysis conducted on concrete elements in both specimens reveal that the mesh size has a minimal impact on the overall shape of the force-displacement response in terms of peak forces and loading/unloading slopes, however, it does have a significant influence on the residual drifts. The results of the mesh sensitivity analysis of concrete elements in terms of residual drifts for specimens with and without ED bars are shown in Figure 12(a) and (b), respectively. The residual drifts were obtained from the hysteretic curve when the column was unloaded at the zero force point.

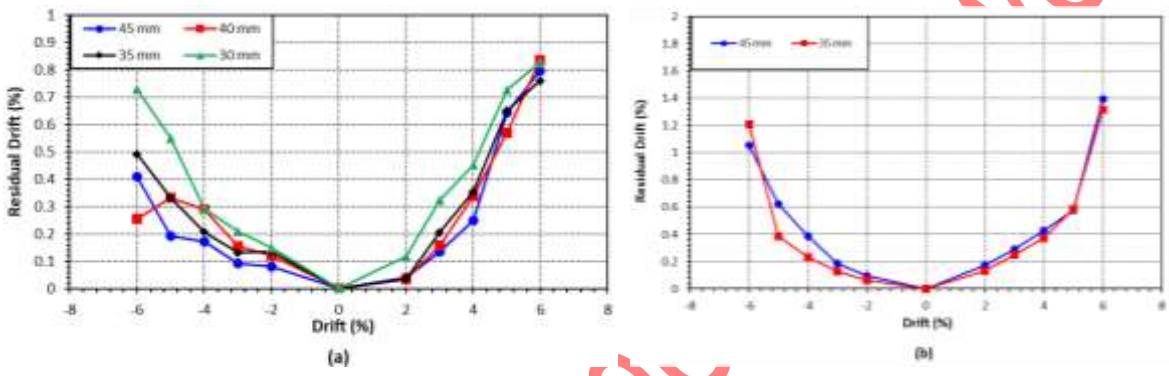

Figure 12 Sensitivity of residual drifts to concrete elements mesh size for specimens (a) without ED bars (b) including ED bars

The results show that the residual drifts in specimens with no ED bars are more sensitive to the mesh size. This is because there are no bonded bars in this specimen and therefore all the forces are transferred through the concrete. Excessive stress values in concrete members result in element distortion and discrepancy in results. On the other hand, a uniform distribution of forces between concrete and ED bars in specimen with ED bars provides more robust results. Due to the fact that the applied drift ratio is loaded first in the positive direction and then in the negative direction, asymmetric residual drifts are produced in both columns. The asymmetry in residual drifts for specimen without ED bars is more prominent, especially at larger mesh sizes where element distortion occurs as shown in Figure 12(a). In contrast, the presence of ED bars in specimen with ED bars leads to reduced asymmetry in residual drifts as shown in Figure 12(b). Consequently, a finer mesh was adopted for specimens without ED bars to ensure the reliability of the results in this study. Thus, mesh sizes of 45 and 35 mm were selected for specimens with and without ED bars, respectively. It is worth noting that although the results of the mesh sensitivity analysis of the specimen without ED bars at a mesh size of 30 mm seem more favorable than 35 mm, the computational cost is significantly increased and thus the mesh size of 35 mm was chosen. Furthermore, a mesh size of 30 mm was adopted for ED bar elements based on the results.

3.3 Parametric study

The validated numerical model is used in this section to investigate the effect of different design parameters on the behavior of segmental columns prestressed with Fe-SMA bars. The variable parameters

considered include the effect of total axial load ratio at a constant PT force on the column's behavior, the effect of relative contributions of PT force and gravity force to total axial load ratio, the ratio of ED bars to Fe-SMA bars, the confinement of concrete segments, and the configuration of Fe-SMA bars. The analysis is conducted on 23 column specimens as summarized in Table 7.

Table 7 Characteristics of parametric study specimens

No.	P_G*(%)*	P_{PT}*(%)*	*ED/Fe-SMA ratio*	*Confinement*	*Fe-SMA Configuration*
S1 (Ref)	12.5	7.5	0	-75S_{1-4}	D240
S2	10	7.5	0	-75S_{1-4}	D240
S3	15	7.5	0	-75S_{1-4}	D240
S4	17.5	7.5	0	-75S_{1-4}	D240
S5	20	7.5	0	-75S_{1-4}	D240
S6	12.5	7.5	0	-75S_{1-4}	D240
S7	15	5	0	-75S_{1-4}	D240
S8	17.5	2.5	0	-75S_{1-4}	D240
S9	10	7.5	0.18	-75S_{1-4}	D240
S10	10	7.5	0.45	-75S_{1-4}	D240
S11	10	7.5	0.7	-75S_{1-4}	D240
S12	10	7.5	0.85	-75S_{1-4}	D240
S13	20	7.5	0.18	-75S_{1-4}	D240
S14	20	7.5	0.45	-75S_{1-4}	D240
S15	20	7.5	0.7	-75S_{1-4}	D240
S16	20	7.5	0.85	-75S_{1-4}	D240
S17	12.5	7.5	0	-75S_{1-4}	D240
S18	12.5	7.5	0	-150S_{1-4}	D240
S19	12.5	7.5	0	-37.5S_{1-4}	D240
S20	12.5	7.5	0	-37.5/S_{2-4}-75S_1	D240
S21	12.5	7.5	0	/S_{2-4}-75J_1	D240
S22	12.5	7.5	0	-75S_{1-4}	D240
S23	12.5	7.5	0	-75S_{1-4}	D50

Note: 1- P_G is gravity load ratio which is defined as $P_G = \frac{F_g}{(f_c' A_g)}$ where F_g is the dead load on the column, f_c' is the concrete strength, and A_g is the gross section area of the column. 2- P_{PT} is prestressing load ratio which is defined as $P_{PT} = \frac{F_{PT}}{(f_c' A_g)}$ where F_g is the total prestressing force on the column applied by Fe-SMA bars. 3- The confinement is given in the notation $A_{b-c} - D$, where A denotes the confining element (S for spiral and J for jacket), subscripts b and c denotes the number of segments, and D denotes the spacing of spirals. 4- The configuration of Fe-SMA bars is indicated by D240 and D50, with the number representing the distance of each bar from the center of the section.

The results of the parametric study are mainly discussed in terms of residual drifts, and equivalent viscous damping ratio (EVDR), at each drift ratio, as the focus of this study is on the self-centering and energy dissipation capacity of Fe-SMA prestressed segmental columns. The force-displacement hysteresis of each specimen was processed to obtain this information. The 1.0% residual drift limit proposed by the Japan Road Association (JRA) is plotted on the residual drift graphs.Note that the EVDR is used to quantitatively express the energy dissipation capacity of the specimens as expressed by Equation 10 [79].

$$\xi_{eq} = \frac{A_h}{2\pi V_m \Delta_m} = \frac{A_h}{4\pi A_e} \quad (10)$$

Where V_m and Δ_m represent the average peak force and displacement values, and A_h is the energy dissipated per cycle, which is obtained from the area enclosed by the hysteretic curve at each cycle, and A_e is elastic strain energy of the system with secant stiffness $k_{eff} = V_m/\Delta_m$.

3.3.1 Effect of total axial load ratio at constant PT force

Five numerical analyses were conducted on specimens S1 to S5 to investigate the effect of total axial load ratio on the behavior of prestressed segmental columns with Fe-SMA. The total axial load ratio was varied by changing the gravity load ratio from 10% to 20% at a constant PT axial load ratio of 7.5%, as shown in Table 7. Figure 13(a) shows that the residual drifts increase by 1.5 and 4 times at drift ratios of 2 and 6%, respectively, in the positive direction on increasing the axial load ratio by 10%. Furthermore, the EVDR approximately doubles as axial load ratio increases from 10 to 20%, as shown in Figure 13(b). This is mainly because the axial force generated by gravity causes the P-Δ phenomenon, which increases the moment at the base of the column, further aggravating the damage to the concrete and reducing the lateral load capacity. More damage to the concrete means a higher energy dissipation and therefore higher residual drifts. In summary, increasing the axial force increases the energy dissipation capacity, while significantly reduces the self-centering behavior of the column.

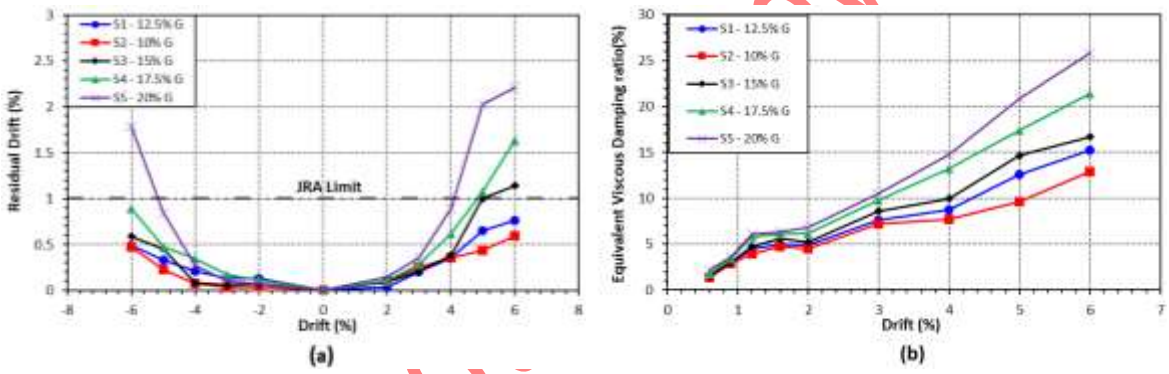

Figure 13 Effect of total axial load ratio at constant PT force on (a) the residual drift (b) the equivalent viscous damping ratio of Fe-SMA prestressed segmental columns

3.3.2 Effect of relative contributions of PT force and gravity force to total axial load ratio

The effect of the contribution of each component of axial load ratio on the column behavior is examined through specimens, S6, S7, and S8. The specimens have a fixed total axial load ratio of 20% while the gravity and PT load contributions are varied, as shown in Table 7. Figure 14(a) shows the residual drift values of three specimens at each drift ratio. It can be observed that the specimens exhibit similar behavior up to 3% drift ratio due to the identical total axial load ratio. However, from 4% drift ratio, the residual drift values begin to increase as the P-Δ effect becomes significant for specimens with higher gravity load. Specimen S8 with the highest gravity load ratio, over 75% of the total axial load ratio, experienced residual drifts greater than 1% and approximately double than that of the other two specimens at 6% drift, as shown in Figure 14(a). A similar trend was observed in the EVDR values. As such, up to a 3% drift ratio, all specimens exhibited comparable behavior but began to show different behavior from 4% drift ratio, as shown in Figure 14(b). The maximum EVDR value for specimen S8 at 6% drift ratio was approximately 21%, compared to 15% for S6. In general, it can be concluded that the column with the higher contribution of PT load (about 35 to 40% of the total axial load ratio) performs better in terms of self-centering. This is because it provides the compressive axial load necessary to clamp the segments together without causing the P-Δ effect.

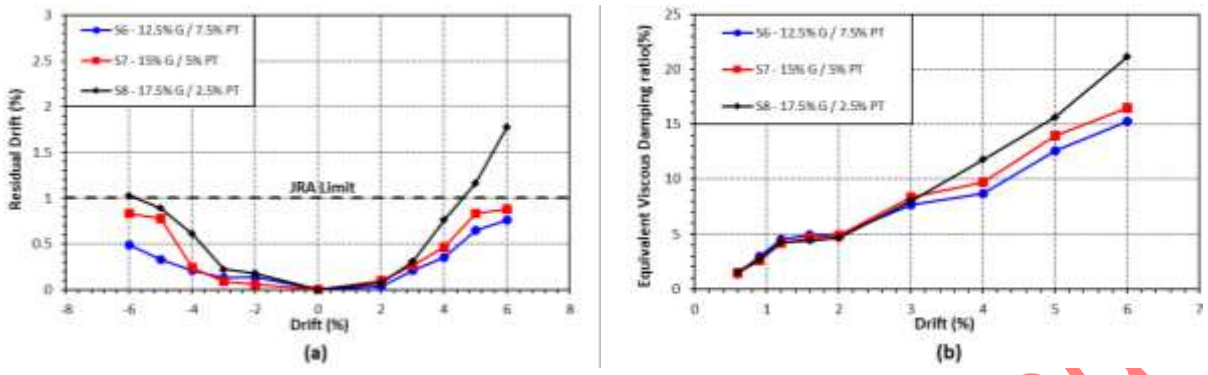

Figure 14 Effect of relative contributions of PT force and gravity force to total axial load ratio on (a) the residual drift (b) the equivalent viscous damping ratio of Fe-SMA prestressed segmental columns

3.3.3 Effect of ratio of ED bars to Fe-SMA bars

Segmental columns with only prestressing reinforcements suffer from poor energy dissipation capacity despite their excellent self-centering behavior. This section examines the effect of different ED bar ratios on the cyclic behavior of segmental columns prestressed with Fe-SMA bars under low and high axial load ratios. Eight specimens with different ED/Fe-SMA reinforcement ratios were considered, four specimens with 10% gravity load ratio and four specimens with 20% gravity load ratio at a constant PT load ratio of 7.5%, denoted as S9 to S16, as shown in Table 7. To eliminate the effect of ED bar configuration, the number and arrangement of ED bars were kept the same and the ratio was changed by altering the diameter of the bars. Eight mild steel bars with sizes of 10, 16, 20, and 22 mm were used to achieve ED bar to Fe-SMA ratios of 0.18, 0.45, 0.7, and 0.85, respectively. The bars have a length of 2660 mm and start from 700 mm below the footing surface to the center of the third segment. The bars are fully constrained in the surrounding concrete as described in Section 2.3. 200 mm of the ED bars are left unbonded below the first joint (footing-Seg1) to avoid strain concentration and fracture of bars [5,15,80].

Figure 15 shows an increase in residual drift as the ratio of ED/Fe-SMA reinforcement increases from 0.18 to 0.85. This is because the moment induced by the plastic deformation of the ED bars increases relative to the self-centering moment caused by the gravity and the PT forces. A higher ratio of ED bars results in a larger plastic moment and therefore larger residual displacements. Figure 15(a) and (c) shows that the residual drift for specimens with 10% gravity load ratio increased by 3.9 and 2.8 times at drift ratios of +4 and +6%, respectively, with the increase in ED/Fe-SMA reinforcement ratio from 0.18 to 0.85. For specimens with 20% gravity load ratio, however, the increase is smaller, as shown in Figure 15(b) and (d). At drift ratios of +4% and +6%, the residual drifts increased by 2 and 1.3 times, respectively, as the ED/Fe-SMA ratio increased from 0.18 to 0.85. The reason for the smaller variation in residual drifts on increasing the ED/Fe-SMA ratio in specimens with 20% gravity load ratio is due to the fact that higher axial load causes higher axial strains in concrete and ED bars and more loss of prestressing in Fe-SMA bars. Of these three factors, excessive concrete damage is more significant and therefore dominantly responsible for large residual drifts.

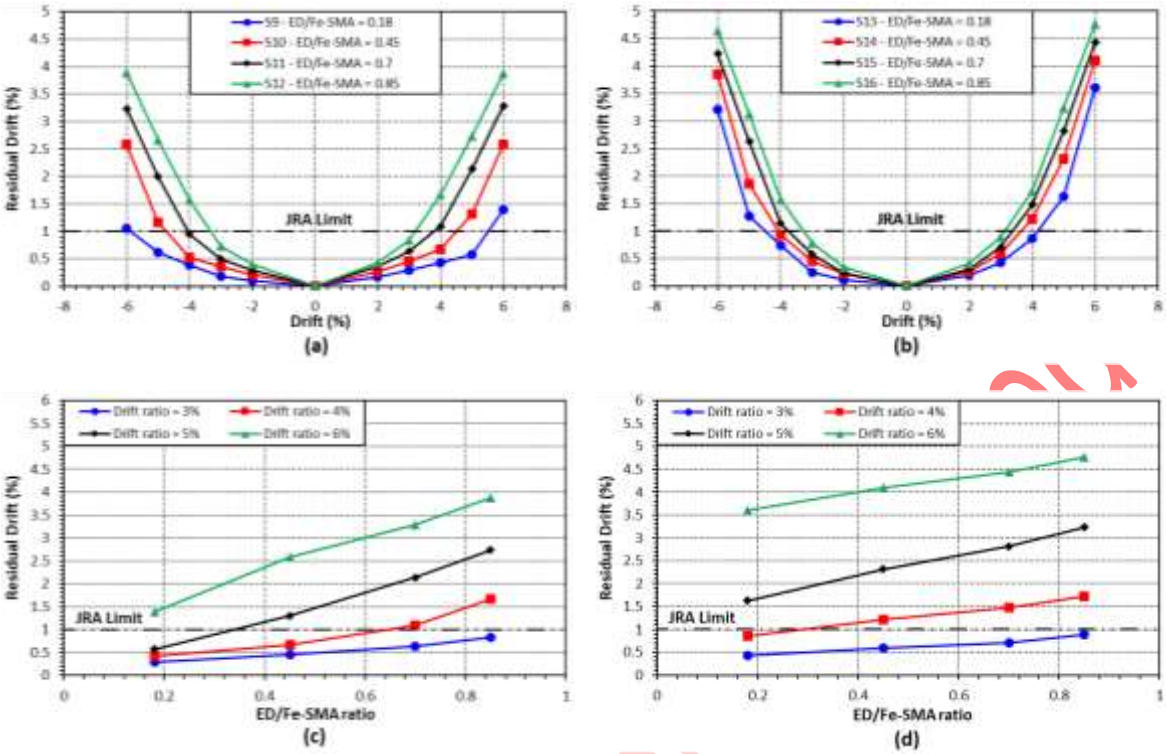

Figure 15 Effect of ED/Fe-SMA reinforcement ratio on the residual drift of Fe-SMA prestressed segmental columns with (a)& (c) 10% gravity force ratio (b)&(d) 20% gravity force ratio

The plastic deformation of ED bars and more concrete damage also result in higher energy dissipation capacity. Figure 16 shows that with increasing the ED/Fe-SMA from 0.18 to 0.85, the maximum EVDR increased from 17 to 29% and from 27 to 35% for specimens with 10 and 20% gravity load ratio, respectively. In other words, the EVDR improved by 71% for 10% gravity load ratio and only 29% in the case of 20% gravity load ratio for the same reason as described for the residual drifts. The EVDR plots of specimens S2 and S5, with the same axial load ratio and no ED bars, are also shown in Figure 16(a) and (b). The maximum EVDR for S2 and S5 is 13% and 26%, respectively. Previous experimental studies showed that a typical segmental column with only prestressing tendons has a maximum EVDR of around 6% at 5% drift which is inadequate, and this value can be enhanced up to a value of 22% ratio by adding ED bars [5,81]. In the current study at a similar total axial load ratio, a maximum EVDR of around 10% was observed at 5% drift for Fe-SMA prestressed columns without any ED bars, which is about 40% higher than conventional segmental columns without ED bars. This means that Fe-SMA bars not only provide self-centering thorough prestressing in segmental columns but also provide energy dissipation capacity even without additional ED devices compared to segmental columns post-tensioned with conventional tendons. This is because tendons remain elastic until large drift levels due to their high yield strength and make a negligible contribution to energy dissipation, while Fe-SMAs yield at lower drifts and begin to contribute to energy dissipation (owing to their high ductility) after losing the prestressing. This implies that Fe-SMA prestressed segmental columns would require a minimal amount of ED bars to satisfy the energy dissipation requirements as opposed to conventionally prestressed columns.

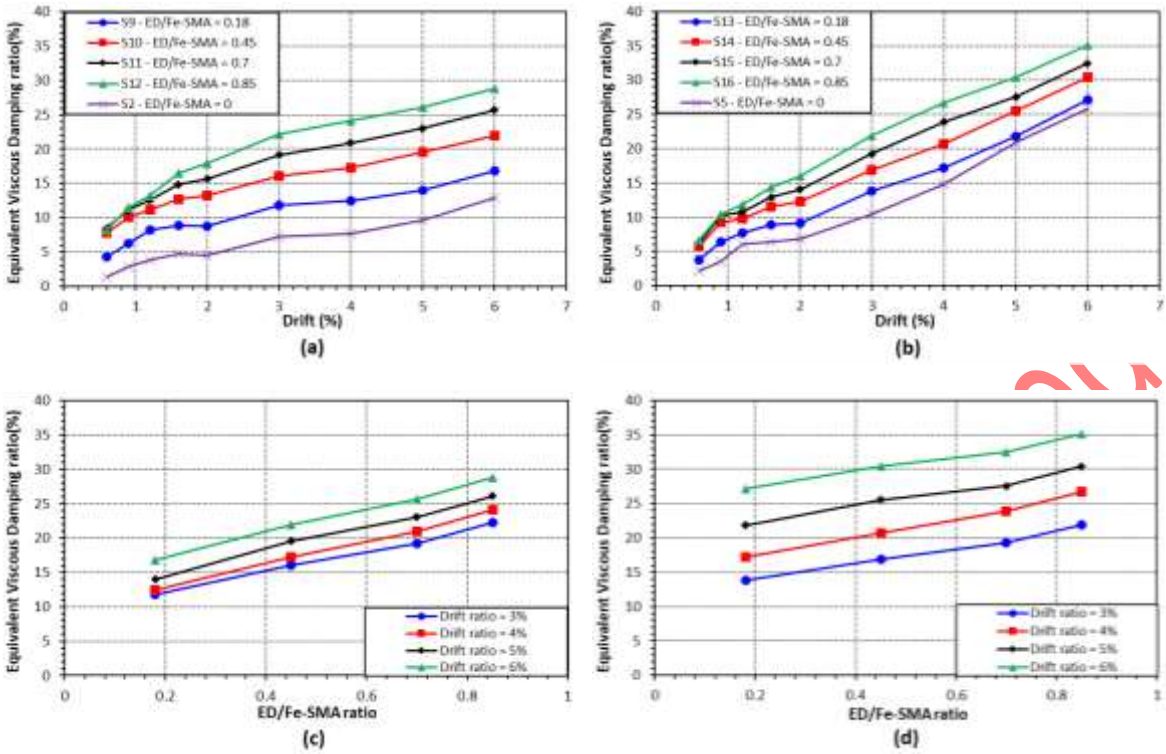

Figure 16 Effect of ED/Fe-SMA reinforcement ratio on the the equivalent viscous damping ratio of Fe-SMA prestressed segmental columns with (a)& (c) 10% gravity force ratio (b)&(d) 20% gravity force ratio

3.3.4 Effect of concrete confinement

Due to the rocking behavior of precast segmental columns, high axial compressive strains are expected at the toes of the base segment. Therefore, several confinement methods have been proposed in previous studies to prevent damage at these regions. This study investigates the effectiveness of five confinement techniques, including variable spacing of spirals and installation of a 6 mm steel jacket at the base segment by conducting analysis on specimens S17 to S21, as shown in Table 7. Three different spiral spacings of 37.5, 75, and 150 mm were considered to understand the effect of spiral spacing on the confinement of the base segment. The results show that by reducing the spiral spacing by 4 times, the residual drifts significantly reduces, as shown in Figure 17(a). For instance, the maximum residual drift at a drift ratio of +6% decreased from 2.52% to 0.2%, which is well below the self-centering limit. However, smaller residual drifts imply less concrete damage and therefore less energy dissipation. This can be clearly seen in Figure 17(b), where reducing the spiral spacing reduces the maximum EVDR from 17.5% to 11%. The installation of the steel jacket further improved the self-centering behavior by reducing the residual drifts to the order of 0.1%, as shown in Figure 17(a). As expected, the maximum EVDR was reduced to about 10%, which is still at the satisfactory EVDR limit of 10%. In other words, the results of specimens S20 and S21 in Figure 17(a) show that the steel jacket can provide more effectively concrete confinement than closely spaced spirals, although it may be more expensive. By comparing the results of specimens S19 and S20, which have identical spiral spacing for the bottom segment and different spacing for the top segments, in Figure 17(a) and (b), it can be concluded that these two specimens have completely similar behavior, indicating that the confinement of the top segments is not as effective as the confinement of the bottom segment. Figure 18 compares the hysteresis graphs of specimens S18 and S21. The effect of concrete confinement is clearly evident on peak strength, strength loss, and residual drift. To summarize, it is concluded that

using a steel jacket or a close arrangement of spirals at the base segment improves the self-centering behavior, but affects the energy dissipation capacity of the column.

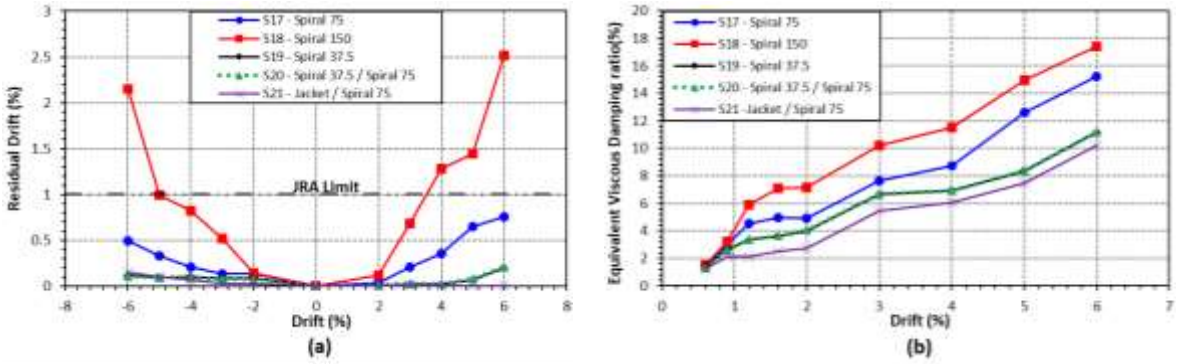

Figure 17 Effect of concrete confinement on (a) the residual drift (b) the equivalent viscous damping ratio of Fe-SMA prestressed segmental columns

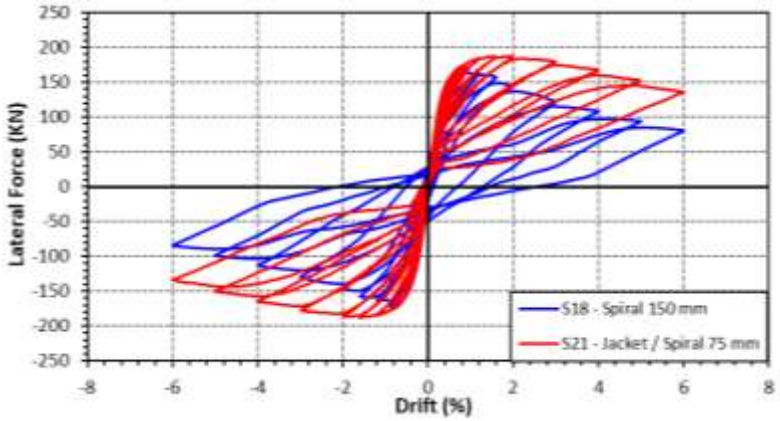

Figure 18 Effect of concrete confinement on hysteresis curve of Fe-SMA prestressed segmental columns

3.3.5 Effect of configurations of Fe-SMA bars

Another factor that could possibly influence the cyclic behavior of concrete segmental columns is the arrangement of the prestressing reinforcement in the cross-section. A limited amount of research has been conducted in this regard for steel tendons. In the case of Fe-SMA, the arrangement in the section is more important because they have a lower yield strength than steel tendons, and placing them away from the center can lead to early yielding and loss of prestressing force. To investigate the role of Fe-SMA arrangement on the cyclic behavior of the prestressed segmental columns, two models, S22 and S23, with central and circumferential arrangement of Fe-SMA bars were considered, as shown in Table 7. Specimen S22 contains Fe-SMA bars at a distance of 240 mm from the center as shown in Figure 19(a), while in specimen S23 Fe-SMA bars were placed at a distance of 50 mm from the center, as shown in Figure 19(b). The results in Figure 20(a) show that the residual drifts of the specimen with the central arrangement of Fe-SMA bars is significantly higher than that of the specimen with circumferential arrangement by 1.5 and 4.3 times at +3% and +6% drift ratios, respectively. In addition, the maximum EVDR also increased from 15.2% to 21.7% as the arrangement was changed from circumferential to central, as shown in Figure 20(b). The higher residual drifts and EVDR values in the specimen with central arrangement of bars is because

the concrete at the extreme fibers carries all the stresses/strains itself and undergoes more damage, whereas in the specimen with circumferential arrangement, the Fe-SMA bars carry some of the stresses/strains and thus causes less damage to the concrete. In addition, the Fe-SMA bars elongate more in the case of the circumferential arrangement, which induces higher stress in the bars and thus higher PT force. Figure 21 compares the stress level induced in Fe-SMA bars #5 and #8 (refer to Figure 19) in the specimens with two bar configurations. Figure 21 confirms that the circumferential arrangement of bars results in higher tensile stress values for both central (Fe-SMA #5) and outermost (Fe-SMA #8) bars by 1.14 and 1.16 times at +6% drift ratio, respectively. When the bar is loaded to drift ratios larger than 2% on the push side, the Fe-SMA #8 in the circumferential arrangement (S22) experiences compressive stresses while the Fe-SMA #8 in the central arrangement (S23) retains its prestressing force, as shown in Figure 21(a).

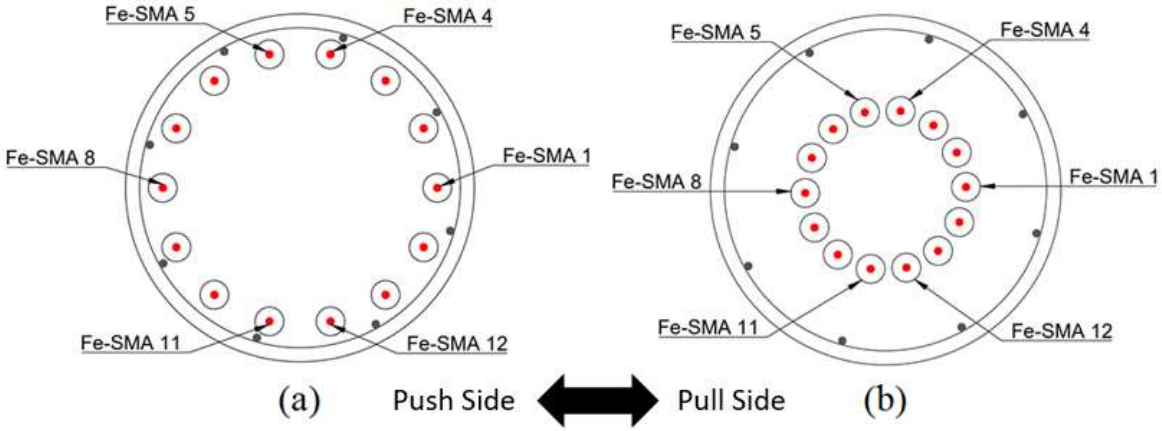

Figure 19 Arrangement of Fe-SMA bars in (a) specimen S22 (b) specimen S23

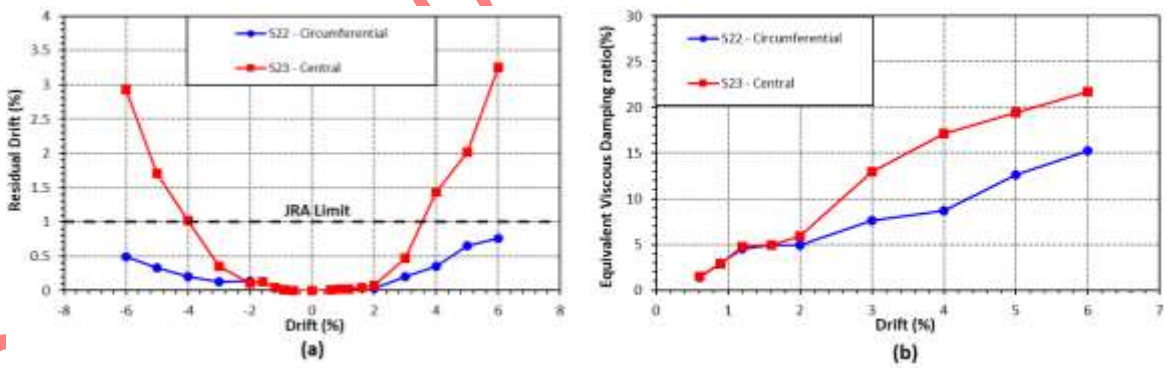

Figure 20 Effect of configurations of Fe-SMA bars on (a) the residual drift (b) the equivalent viscous damping ratio of Fe-SMA prestressed segmental columns

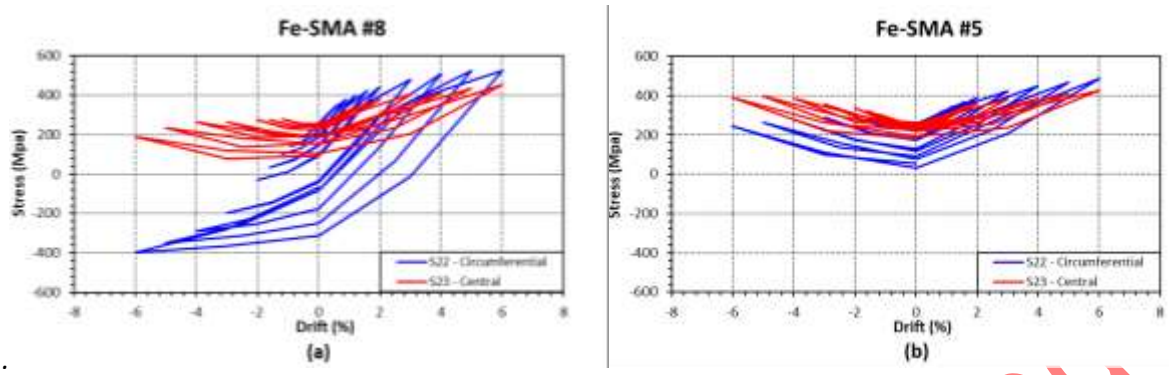

Figure 21 Effect of configurations of Fe-SMA bars on induced stress level of (a) Fe-SMA #8 (b) Fe-SMA #5

As a result of the higher stress levels in the Fe-SMA bars and the larger moment arm in the circumferential bar specimen, the peak lateral strength increased by almost 10 KN, as shown in Figure 22 (a). In addition, the strength degradation, as shown in Figure 22(b), decreased from about 61% to 41% at the maximum drift ratio because less damage was induced in the concrete. Figure 23 shows that in both configuration of Fe-SMA bars, less total prestressing force remains in the columns when they are unloaded to their original position after loading to high drift ratios. This is because activated Fe-SMA bars exposed to a strain range limit of 0.4-0.5% lose their total recovery stress [69]. According to Figure 23, specimen S22 with circumferential arrangement lost its total prestressing force after loading to +4% drift ratio, while specimen S23 lost only 50% of its total prestressing force until 6% drift. In general, it can be concluded that the placement of Fe-SMA bars on the circumference significantly improves the self-centering behavior and provides an acceptable EVDR value higher than 10%. In addition, the performance of the column is enhanced in terms of lateral strength and strength degradation despite the loss of total prestressing at a relatively lower drift ratio.

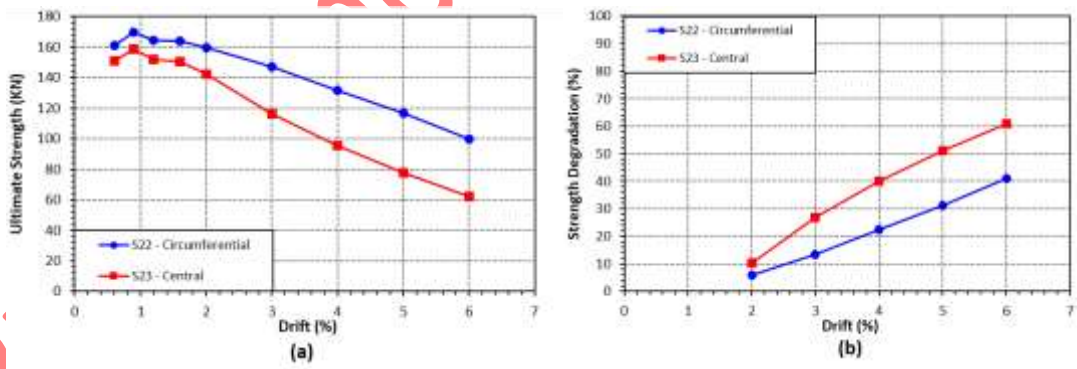

Figure 22 Effect of configurations of Fe-SMA bars on (a) the ultimate lateral strength (b) the strength degradation of Fe-SMA prestressed segmental columns

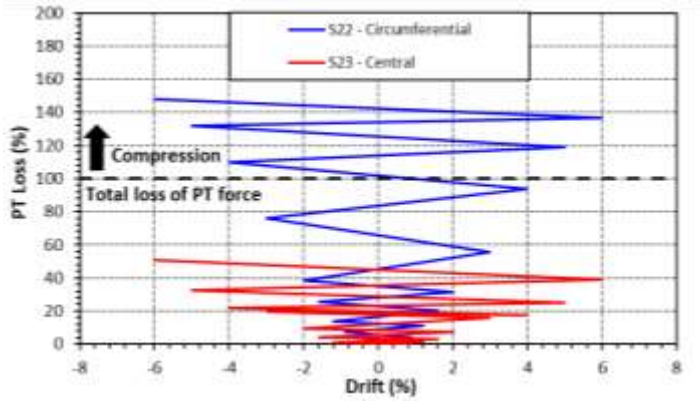

Figure 23 Effect of configurations of Fe-SMA bars on total prestressing force of Fe-SMA prestressed segmental columns

4 Self-centering criteria for Fe-SMA Prestressed Segmental Columns

The Commentary of Design Specifications for Highway Bridges (Part V, Section 6.4.6) [2] states that the residual drift ratio for bridge piers is required to be less than 1% so that the bridge structures can be reparable after a seismic event. A number of re-centering criteria have been proposed that are capable of predicting the self-centering capacity of columns, which are explained as follows.

4.1 Self-centering Criteria by Ou et al.

Ou et al. [5] proposed a factor λ_{ED} which represents the contribution of ED bars to the total lateral strength of the column, as expressed by Equation 11. It was recommended that the λ_{ED} should not exceed 35% to maintain self-centering capability [5].

$$\lambda_{ED} = \frac{V_{exp} - V_{exp0}}{V_{exp}} \qquad 11$$

where V_{exp} is the lateral strength of the column including ED bars and V_{exp0} is the lateral strength of the column without the ED bars.

The values of λ_{ED} are calculated for specimens with ED bars in this study and presented in Table 8. The residual drift values of specimen S9 to S16 are summarized in Table 9 to facilitate comparison of the different self-centering criteria. By comparing the results of Table 8 and the average residual drift of the specimens S9 to S16 in Table 9, it can be concluded that the proposed criterion is overestimating the self-centering capability of columns specifically at high drift ratios. For example for specimens S13 and S14 at 6% drift ratio, the self-centering ratio has a value of less than 35%, however, the residual drifts are a lot larger than 1%, as shown in Table 9.

Table 8 Values of re-centering ratio proposed by Ou et al. [5] for Fe-SMA prestressed segmental columns

	Self-Centering Ratio λ_{ED}							
Drift (%)	10% gravity load ratio				20% gravity load ratio			
	S9	S10	S11	S12	S13	S14	S15	S16
3	3.5	19.2	25.7	31.6	-2.2	18.0	23.8	29.4
4	2.3	19.3	25.8	32.3	-2.8	20.0	26.6	33.0
5	2.0	20.2	26.3	33.6	-2.6	23.5	31.2	37.8

6	7.7	19.8	26.9	34.7	11.4	27.1	36.1	43.7

Table 9 Average values of residual drift for specimen with ED bars

	Residual Drift (%)							
Drift (%)	10% gravity load ratio				20% gravity load ratio			
	S9	S10	S11	S12	S13	S14	S15	S16
3	0.24	0.41	0.56	0.78	0.34	0.53	0.65	0.83
4	0.40	0.60	1.02	1.62	0.80	1.07	1.31	1.64
5	0.60	1.23	2.06	2.70	1.45	2.09	2.72	3.18
6	1.22	2.58	3.26	3.88	3.41	3.98	4.33	4.71

4.2 Self-centering Criteria by Hieber et al.

The self-centering criterion, proposed by Hieber et al [82], is based on the ratio of the self-centering forces, including gravity load and prestressing force, to the total resisting force of the ED bars when the column is at the origin (Equation 12). This is because the critical position for self-centering is when the column is close to the vertical position and the stress in the prestressing elements is at a minimum for that cycle [83].

$$\lambda_{rc} = \frac{P_{col} + A_p f_{p0}}{A_s f_y} \qquad 12$$

Where, P_{col} is axial gravity load, A_p is the area of prestressing elements, f_{p0} is the stress in prestressing elements, A_s is the area of ED bars, and f_y the yield strength of ED bars.

According to this criteria, the column is considered self-centering for λ_{rc} values greater than unity. The λ_{rc} values for specimens S9 to S16 are summarized in Table 10. By comparing the results of Table 10 and Table 9, It can be concluded that the proposed criterion can reasonably predict the self-centering capability of specimens with 10% gravity load ratio. However, it overestimates the self-centering capability of specimens with 20% gravity load ratio at high drift ratios. This is because in this criterion, higher gravity load ratio results in higher self-centering ratio regardless of its P-Δ effect. Whereas in fact the P-Δ effect causes more concrete damage and higher residual drifts at high drift ratios.

Table 10 Values of re-centering ratio proposed by Hieber et al [82] *for Fe-SMA prestressed segmental columns*

	Self-Centering Ratio λ_{rc}							
Drift (%)	10% gravity load ratio				20% gravity load ratio			
	S9	S10	S11	S12	S13	S14	S15	S16
3	6.3	2.5	1.7	1.2	11.6	4.6	3.0	2.1
4	5.1	2.1	1.4	1.0	10.9	4.3	2.8	1.9
5	4.2	1.7	1.1	0.8	10.3	4.1	2.6	1.8
6	3.5	1.5	1.0	0.7	9.8	3.8	2.5	1.7

4.3 Self-centering criteria by Wang et al.

Wang et al. [6] proposed a self-centering criterion that evaluates the self-centering capacity of the column as the ratio of the self-centering moment to the resisting moment induced by the ED bars (Equation 13) at a given drift ratio. The moments are taken at the center of the concrete compression block. The self-centering moment is expressed by Equation 14, and consists of contributions from gravity load and prestressing force. The resisting moment is the sum of the moments induced by each ED bar as expressed by Equation 15. Columns with self-centering factor values greater than 1.25 are considered to have sufficient self-centering capacity [6]. The values of λ_{SC} are calculated and presented in Table 11 for specimens S9 to S16.

$$\lambda_{SC} = \frac{M_{SC}}{M_{ED}} \tag{13}$$

$$M_{SC} = FL - M_{ED} = P_G\left(\frac{h}{2} - \Delta - d_{FC}\right) + P_{PT}\left(\frac{h}{2} - d_{FC}\right) \tag{14}$$

$$M_{ED} = \sum_{i=1}^{n} F_{ED,i}\left(d_{ED,i} - d_{Fc}\right) \tag{15}$$

Where FL is the total moment at the section, P_G is the gravity load, P_{PT} is the prestressing force, Δ is the applied drift ratio, h is the height of the column section, d_{FC} is the centroid of the concrete compression block to the outermost fiber of the compression zone, $F_{ED,i}$ is the force of the target ED bar at the distance $d_{ED,i}$ from the outermost fiber of the compression zone. It is worth noting that P_{PT} in Equation 14 is the total PT force induced in the elongated Fe-SMA bars at the applied drift ratio.

By comparing the results of Table 11 and Table 9, it can be concluded that the criterion is accurate in predicting the self-centering capacity of specimens. However, it has been observed that the self-centering criterion overestimates self-centering capability at high drift ratios. A notable example is specimen S9, where, at 6% drift ratio, the self-centering ratio is more than 1.25, while the residual drift is larger than 1%. It was noted in [6] that self-centering ratios greater than 1.25 do not necessarily lead to residual drifts less than 1%. This is because residual drifts are not solely dependent on self-centering ratios, but also on the maximum applied drift ratio. The residual drift can only be prevented from exceeding 1% when the SC factor is above 1.25, if the maximum drift does not exceed 4% [6].

Table 11 Values of re-centering ratio proposed by Wang et al. [6] for Fe-SMA prestressed segmental columns

	Self-Centering Ratio λ_{sc}							
Drift (%)	10% gravity load ratio				20% gravity load ratio			
	S9	S10	S11	S12	S13	S14	S15	S16
3	6.8	2.7	1.7	1.2	7.7	3.0	1.8	1.3
4	5.5	2.1	1.4	0.9	5.4	2.1	1.3	0.9
5	4.2	1.7	1.0	0.7	3.2	1.2	0.7	0.5
6	3.0	1.2	0.7	0.5	1.1	0.4	0.2	0.1

5 Conclusions

This study proposed a novel segmental column concept where prestressing is achieved through the unique self-prestressing characteristics of Fe-SMA. The seismic behavior of the proposed prestressed segmental columns was evaluated by developing a nonlinear finite 3D element model of the column. The developed model was validated against the experimental results available from the previous studies. The material behavior of activated and non-activated Fe-SMA bars subjected to cyclic tension/compression reversals was incorporated in the FE model. The validated FE model of the columns was used to perform a comprehensive parametric study wherein the effect of various parameters including total axial load ratio at constant PT force, relative contributions of PT force and gravity force to total axial load ratio, ratio of ED bars to Fe-SMA bars, confinement of concrete segments, and configuration of Fe-SMA bars on the performance of precast segmental columns prestressed with Fe-SMA bars was investigated. Based on the results of this study, the following conclusions are drawn:

1. The combined isotropic/kinematic hardening method using the stabilized cycle approach was able to model the stress-strain behavior of activated and non-activated Fe-SMA under cyclic tension-compression reversals with reasonable accuracy. The modeling results were in good agreement with the experimental results in terms of peak stresses and loading/unloading slope.
2. The prestressed Fe-SMA bars can provide both self-centering and energy dissipation capacity to segmental columns compared to conventional tendons, which typically provide only self-centering capacity and need additional measures for enhancing the energy dissipation capacity. Whilst the EVDR is typically in the range of 5-6% for conventional segmental columns, the Fe-SMA prestressed segmental columns showed maximum EVDR higher than 10% with no additional ED devices. This is because Fe-SMAs yield during loading and contribute to energy dissipation due to their high ductility, while tendons remain elastic during loading, and thus make a negligible contribution to the energy dissipation.
3. The amount of gravity and prestressing load on the column is an important parameter affecting the residual drift and energy dissipation capacity of Fe-SMA prestressed segmental columns. While prestressing load helps in self-centering, the higher gravity load results in P-Δ moment, which accelerates the lateral strength degradation and increases the residual drift and energy dissipation capacity of the column. Therefore, the gravity and prestressing loads must be carefully designed to achieve an adequate self-centering and energy dissipation performance. Based on the results, it is concluded that an upper limit of 22.5% for the total axial load ratio and a minimum PT force limit of 35 to 40% of the total axial load ratio at a transverse reinforcement ratio of 0.31% is required to keep the residual drifts less than 1% and the maximum EVDR greater than 10%.
4. The ratio of ED/Fe-SMA reinforcement significantly affected the residual drift and energy dissipation of the columns. With the increase in ED/Fe-SMA reinforcement ratio from 0.18 to 0.85, the average residual drift increased by 3.9 and 2.8 times at target drift ratios of 4% and 6%, respectively. Similarly, the EVDR increased by 93% and 71% at target drift ratios of 4% and 6%, respectively. An ED/Fe-SMA reinforcement ratio of 0.45 resulted in EVDR of greater than 10% in addition to residual drifts smaller than 1% at a target drift of 4%, and is therefore recommended for design.
5. The circumferential arrangement, as opposed to the central arrangement of Fe-SMA bars in the cross-section, significantly improves the self-centering behavior of columns by reducing

the concrete damage. In addition, it results in better performance in terms of peak strength and strength degradation. However, this arrangement may result in an early loss of total prestressing force, despite better self-centering compared to the central arrangement of bars.

References

[1] K. Kawashima, G. A. MacRae, J. Hoshikuma, and K. Nagaya, "Residual Displacement Response Spectrum," *J. Struct. Eng.*, vol. 124, no. 5, pp. 523–530, 1998, doi: 10.1061/(asce)0733-9445(1998)124:5(523).

[2] Japan Road Association (JRA), "DESIGN SPECIFICATIONS FOR HIGHWAY BRIDGES PART V SEISMIC DESIGN," no. March, 2012.

[3] X. Liu, J. Li, H. H. Tsang, and J. L. Wilson, "Evaluating Self-Centering Behavior of Unbonded Prestressed Bridge Columns Using a New Performance Index Based on Quasi-Static Analysis," *J. Earthq. Tsunami*, vol. 12, no. 1, Mar. 2018, doi: 10.1142/S179343111850001X.

[4] W. Y. Kam, S. Pampanin, A. Palermo, and A. J. Carr, "Self-centering structural systems with combination of hysteretic and viscous energy dissipations," *Earthq. Eng. Struct. Dyn.*, vol. 39, no. 10, pp. 1083–1108, Aug. 2010, doi: 10.1002/eqe.983.

[5] Y.-C. Ou, P.-H. Wang, M.-S. Tsai, K.-C. Chang, and G. C. Lee, "Large-Scale Experimental Study of Precast Segmental Unbonded Posttensioned Concrete Bridge Columns for Seismic Regions," *J. Struct. Eng.*, vol. 136, no. 3, pp. 255–264, Mar. 2010, doi: 10.1061/(asce)st.1943-541x.0000110.

[6] Z. Wang, J. Wang, G. Zhao, and J. Zhang, "Design criterion for the self-centering capacity of precast segmental UHPC bridge columns with unbonded post-tensioning tendons," *Eng. Struct.*, vol. 200, p. 109706, Dec. 2019, doi: 10.1016/J.ENGSTRUCT.2019.109706.

[7] D. G. Hieber, J. M. Wacker, M. O. Eberhard, and J. F. Stanton, "Precast concrete pier systems for rapid construction of bridges in seismic regions," 2005.

[8] L. S. Cohagen, J. B. K. Pang, J. F. Stanton, and M. O. Eberhard, "A precast concrete bridge bent designed to re-center after an earthquake," 2008.

[9] J. T. Hewes and M. J. N. Priestley, "Seismic design and performance of precast concrete segmental bridge columns," Dept. of Structural Engineering, University of California, San Diego, La Jolla, Calif. :, 2002.

[10] C. C. Chou and Y. C. Chen, "Cyclic tests of post-tensioned precast CFT segmental bridge columns with unbonded strands," *Earthq. Eng. Struct. Dyn.*, vol. 35, no. 2, pp. 159–175, Feb. 2006, doi: 10.1002/eqe.512.

[11] Y. C. Ou, M. Sen Tsai, K. C. Chang, and G. C. Lee, "Cyclic behavior of precast segmental concrete bridge columns with high performance or conventional steel reinforcing bars as energy dissipation bars," *Earthq. Eng. Struct. Dyn.*, vol. 39, no. 11, pp. 1181–1198, Sep. 2010, doi: 10.1002/eqe.986.

[12] M. A. ElGawady and H. M. Dawood, "Analysis of segmental piers consisted of concrete filled FRP tubes," *Eng. Struct.*, vol. 38, pp. 142–152, 2012, doi: 10.1016/j.engstruct.2012.01.001.

[13] P. Sideris, A. J. Aref, and A. Filiatrault, "Quasi-Static Cyclic Testing of a Large-Scale Hybrid Sliding-

Rocking Segmental Column with Slip-Dominant Joints," *J. Bridg. Eng.*, vol. 19, no. 10, pp. 1–11, 2014, doi: 10.1061/(asce)be.1943-5592.0000605.

[14] M. Tazarv and M. Saiid Saiidi, "Low-Damage Precast Columns for Accelerated Bridge Construction in High Seismic Zones," *J. Bridg. Eng.*, vol. 21, no. 3, pp. 1–13, 2016, doi: 10.1061/(asce)be.1943-5592.0000806.

[15] Z.-Y. Bu, Y.-C. Ou, J.-W. Song, N.-S. Zhang, and G. C. Lee, "Cyclic Loading Test of Unbonded and Bonded Posttensioned Precast Segmental Bridge Columns with Circular Section," *J. Bridg. Eng.*, vol. 21, no. 2, p. 04015043, Feb. 2016, doi: 10.1061/(asce)be.1943-5592.0000807.

[16] Y. Zhang, W. Fan, Y. Zhai, and W. Yuan, "Experimental and Numerical Investigations on Seismic Behavior of Prefabricated Bridge Columns with UHPFRC Bottom Segments," *J. Bridg. Eng.*, vol. 24, no. 8, pp. 1–17, 2019, doi: 10.1061/(asce)be.1943-5592.0001451.

[17] M. ElGawady, A. J. Booker, and H. M. Dawood, "Seismic Behavior of Posttensioned Concrete-Filled Fiber Tubes," *J. Compos. Constr.*, vol. 14, no. 5, pp. 616–628, Oct. 2010, doi: 10.1061/(asce)cc.1943-5614.0000107.

[18] J. C. Wang, Y. C. Ou, K. C. Chang, and G. C. Lee, "Large-scale seismic tests of tall concrete bridge columns with precast segmental construction," *Earthq. Eng. Struct. Dyn.*, vol. 37, no. 12, pp. 1449–1465, Oct. 2008, doi: 10.1002/eqe.824.

[19] H. Roh and A. M. Reinhorn, "Hysteretic behavior of precast segmental bridge piers with superelastic shape memory alloy bars," *Eng. Struct.*, vol. 32, no. 10, pp. 3394–3403, Oct. 2010, doi: 10.1016/j.engstruct.2010.07.013.

[20] E. Nikbakht, K. Rashid, I. Mohseni, and F. Hejazi, "Evaluating seismic demands for segmental columns with low energy dissipation capacity," *Earthq. Struct.*, vol. 8, no. 6, pp. 1277–1297, 2015, doi: 10.12989/eas.2015.8.6.1277.

[21] Q. Zhang and M. S. Alam, "State-of-the-Art Review of Seismic-Resistant Precast Bridge Columns," *J. Bridg. Eng.*, vol. 25, no. 10, 2020, doi: 10.1061/(asce)be.1943-5592.0001620.

[22] Q. Zhang and M. S. Alam, "The Dynamics of Precast Post-Tensioned Rocking Columns," in *Structures Congress 2018: Bridges, Transportation Structures, and Nonbuilding Structures - Selected Papers from the Structures Congress 2018*, 2018, vol. 2018-April, pp. 349–358. doi: 10.1061/9780784481332.031.

[23] D. Marriott, S. Pampanin, and A. Palermo, "Biaxial testing of unbonded post-tensioned rocking bridge piers with external replacable dissipaters," *Earthq. Eng. \& Struct. Dyn.*, vol. 40, no. 15, pp. 1723–1741, 2011.

[24] D. Marriott, S. Pampanin, and A. Palermo, "Quasi-static and pseudo-dynamic testing of unbonded post-tensioned rocking bridge piers with external replaceable dissipaters," *Earthq. Eng. Struct. Dyn.*, vol. 38, no. 3, pp. 331–354, Mar. 2009, doi: 10.1002/eqe.857.

[25] K. Kawashima, R. Zafra, T. Sasaki, K. Kajiwara, and M. Nakayama, "Effect of polypropylene fiber reinforced cement composite and steel fiber reinforced concrete for enhancing the seismic performance of bridge columns," *J. Earthq. Eng.*, vol. 15, no. 8, pp. 1194–1211, Dec. 2011, doi: 10.1080/13632469.2011.569051.

[26] Y. Zhang and D. Dias-da-Costa, "Seismic vulnerability of multi-span continuous girder bridges with

steel fibre reinforced concrete columns," *Eng. Struct.*, vol. 150, pp. 451–464, Nov. 2017, doi: 10.1016/j.engstruct.2017.07.053.

[27] C. A. Cruz Noguez and M. S. Saiidi, "Performance of Advanced Materials during Earthquake Loading Tests of a Bridge System," *J. Struct. Eng.*, vol. 139, no. 1, pp. 144–154, 2013, doi: 10.1061/(asce)st.1943-541x.0000611.

[28] S. Motaref, M. S. Saiidi, and D. Sanders, "Shake Table Studies of Energy-Dissipating Segmental Bridge Columns," *J. Bridg. Eng.*, vol. 19, no. 2, pp. 186–199, Feb. 2014, doi: 10.1061/(asce)be.1943-5592.0000518.

[29] W. Trono, G. Jen, M. Panagiotou, M. Schoettler, and C. P. Ostertag, "Seismic Response of a Damage-Resistant Recentering Posttensioned-HYFRC Bridge Column," *J. Bridg. Eng.*, vol. 20, no. 7, p. 04014096, Jul. 2015, doi: 10.1061/(asce)be.1943-5592.0000692.

[30] Y. Zhang, W. Fan, Y. Zhai, and W. Yuan, "Experimental and Numerical Investigations on Seismic Behavior of Prefabricated Bridge Columns with UHPFRC Bottom Segments," *J. Bridg. Eng.*, vol. 24, no. 8, p. 04019076, 2019, doi: 10.1061/(asce)be.1943-5592.0001451.

[31] K. S. Youm, J. young Cho, Y. H. Lee, and J. J. Kim, "Seismic performance of modular columns made of concrete filled FRP tubes," *Eng. Struct.*, vol. 57, pp. 37–50, Dec. 2013, doi: 10.1016/j.engstruct.2013.09.001.

[32] Y. C. Ou, Y. Oktavianus, and M. Sen Tsai, "An emulative precast segmental concrete bridge column for seismic regions," *Earthq. Spectra*, vol. 29, no. 4, pp. 1441–1457, 2013, doi: 10.1193/082511EQS205M.

[33] Y. Zhang, G. Wu, and D. Dias-da-Costa, "Cyclic loading tests and analyses of posttensioned concrete bridge columns combining cast-in-place and precast segments," *Bull. Earthq. Eng.*, vol. 17, no. 11, pp. 6141–6163, 2019, doi: 10.1007/s10518-019-00714-0.

[34] D. H. Kim, D. Y. Moon, M. K. Kim, G. Zi, and H. Roh, "Experimental test and seismic performance of partial precast concrete segmental bridge column with cast-in-place base," *Eng. Struct.*, vol. 100, pp. 178–188, 2015, doi: 10.1016/j.engstruct.2015.05.034.

[35] Z. Wang *et al.*, "Quasi-static cyclic tests of precast bridge columns with different connection details for high seismic zones," *Eng. Struct.*, vol. 158, no. December 2017, pp. 13–27, 2018, doi: 10.1016/j.engstruct.2017.12.035.

[36] P. Sideris, "Seismic analysis and design of precast concrete segmental bridges," State University of New York at Buffalo, 2012.

[37] P. Sideris, A. J. Aref, and A. Filiatrault, "Large-Scale Seismic Testing of a Hybrid Sliding-Rocking Posttensioned Segmental Bridge System," *J. Struct. Eng.*, vol. 140, no. 6, pp. 1–15, 2014, doi: 10.1061/(asce)st.1943-541x.0000961.

[38] M. Salehi, P. Sideris, and A. B. Liel, "Experimental testing of hybrid sliding-rocking bridge columns under torsional and biaxial lateral loading," *Earthq. Eng. Struct. Dyn.*, vol. 50, no. 10, pp. 2817–2837, 2021, doi: 10.1002/eqe.3474.

[39] M. Salehi, P. Sideris, and A. B. Liel, "Effect of Major Design Parameters on the Seismic Performance of Bridges with Hybrid Sliding–Rocking Columns," *J. Bridg. Eng.*, vol. 25, no. 10, pp. 1–18, 2020, doi: 10.1061/(asce)be.1943-5592.0001616.

[40] C. Czaderski, M. Shahverdi, R. Brönnimann, C. Leinenbach, and M. Motavalli, “Feasibility of iron-based shape memory alloy strips for prestressed strengthening of concrete structures,” *Constr. Build. Mater.*, vol. 56, pp. 94–105, 2014, doi: 10.1016/j.conbuildmat.2014.01.069.

[41] S. Abouali, M. Shahverdi, M. Ghassemieh, and M. Motavalli, “Nonlinear simulation of reinforced concrete beams retrofitted by near-surface mounted iron-based shape memory alloys,” *Eng. Struct.*, vol. 187, no. July 2018, pp. 133–148, 2019, doi: 10.1016/j.engstruct.2019.02.060.

[42] M. Shahverdi, C. Czaderski, and M. Motavalli, “Iron-based shape memory alloys for prestressed near-surface mounted strengthening of reinforced concrete beams,” *Constr. Build. Mater.*, vol. 112, pp. 28–38, 2016, doi: 10.1016/j.conbuildmat.2016.02.174.

[43] S. Raza, J. Michels, B. Schranz, and M. Shahverdi, “Anchorage behavior of Fe-SMA rebars Post-Installed into concrete,” *Eng. Struct.*, vol. 272, no. September, p. 114960, 2022, doi: 10.1016/j.engstruct.2022.114960.

[44] S. Raza, R. Widmann, J. Michels, M. Saiid Saiidi, M. Motavalli, and M. Shahverdi, “Self-centering technique for existing concrete bridge columns using prestressed iron-based shape memory alloy reinforcement,” *Eng. Struct.*, vol. 294, no. July, p. 116799, 2023, doi: 10.1016/j.engstruct.2023.116799.

[45] M. Shahverdi, J. Michels, C. Czaderski, and M. Motavalli, “Iron-based shape memory alloy strips for strengthening RC members: Material behavior and characterization,” *Constr. Build. Mater.*, vol. 173, pp. 586–599, 2018.

[46] O. E. Ozbulut, R. F. Hamilton, M. M. Sherif, and A. Lanba, “Feasibility of self-pre-stressing concrete members using shape memory alloys,” *J. Intell. Mater. Syst. Struct.*, vol. 26, no. 18, pp. 2500–2514, 2015.

[47] S. M. Daghash and O. E. Ozbulut, “Rehabilitation of reinforced concrete structures using shape memory alloys,” in *Geotechnical and Structural Engineering Congress 2016*, 2016, pp. 685–698.

[48] A. Cladera, E. Oller, and C. Ribas, “Pilot experiences in the application of shape memory alloys in structural concrete,” *J. Mater. Civ. Eng.*, vol. 26, no. 11, p. 4014084, 2014.

[49] A. Cladera, B. Weber, C. Leinenbach, C. Czaderski, M. Shahverdi, and M. Motavalli, “Iron-based shape memory alloys for civil engineering structures: An overview,” *Constr. Build. Mater.*, vol. 63, pp. 281–293, 2014.

[50] S. Zareie, A. S. Issa, R. J. Seethaler, and A. Zabihollah, “Recent advances in the applications of shape memory alloys in civil infrastructures: A review,” in *Structures*, 2020, vol. 27, pp. 1535–1550.

[51] B. Schranz, J. Michels, C. Czaderski, M. Motavalli, T. Vogel, and M. Shahverdi, “Strengthening and prestressing of bridge decks with ribbed iron-based shape memory alloy bars,” *Eng. Struct.*, vol. 241, p. 112467, 2021.

[52] M. Rezapour, M. Ghassemieh, M. Motavalli, and M. Shahverdi, “Numerical modeling of unreinforced masonry walls strengthened with Fe-based shape memory alloy strips,” *Materials (Basel).*, vol. 14, no. 11, p. 2961, 2021.

[53] N. Dolatabadi, M. Shahverdi, M. Ghassemieh, and M. Motavalli, “RC Structures strengthened by an iron-based shape memory alloy embedded in a shotcrete layer—Nonlinear finite element modeling,” *Materials (Basel).*, vol. 13, no. 23, p. 5504, 2020.

[54] C. Czaderski, M. Shahverdi, and J. Michels, “Iron based shape memory alloys as shear reinforcement for bridge girders,” *Constr. Build. Mater.*, vol. 274, no. xxxx, p. 121793, 2021, doi: 10.1016/j.conbuildmat.2020.121793.

[55] B. Schranz, P. R. Wagner, C. Czaderski, and M. Shahverdi, “Fibre optic measurements and model uncertainty quantification for Fe-SMA strengthened concrete structures,” *Eng. Struct.*, vol. 256, p. 114005, 2022, doi: 10.1016/j.engstruct.2022.114005.

[56] B. Schranz, C. Czaderski, T. Vogel, and M. Shahverdi, “Bond investigations of prestressed, near-surface-mounted, ribbed memory-steel bars with full bond length,” *Mater. Des.*, vol. 196, no. September, p. 109145, 2020, doi: 10.1016/j.matdes.2020.109145.

[57] B. Schranz, C. Czaderski, T. Vogel, and M. Shahverdi, “Bond behaviour of ribbed near-surface-mounted iron-based shape memory alloy bars with short bond lengths,” *Mater. Des.*, vol. 191, no. March, p. 108647, 2020, doi: 10.1016/j.matdes.2020.108647.

[58] L. A. Montoya-Coronado, J. G. Ruiz-Pinilla, C. Ribas, and A. Cladera, “Experimental study on shear strengthening of shear critical RC beams using iron-based shape memory alloy strips,” *Eng. Struct.*, vol. 200, p. 109680, 2019.

[59] M. Shahverdi, C. Czaderski, P. Annen, and M. Motavalli, “Strengthening of RC beams by iron-based shape memory alloy bars embedded in a shotcrete layer,” *Eng. Struct.*, vol. 117, pp. 263–273, 2016, doi: 10.1016/j.engstruct.2016.03.023.

[60] S. M. Daghash and O. E. Ozbulut, “Bond--slip behavior of superelastic shape memory alloys for near-surface-mounted strengthening applications,” *Smart Mater. Struct.*, vol. 26, no. 3, p. 35020, 2017.

[61] J. Michels, M. Shahverdi, and C. Czaderski, “Flexural strengthening of structural concrete with iron-based shape memory alloy strips,” *Struct. Concr.*, vol. 19, no. 3, pp. 876–891, 2018, doi: 10.1002/suco.201700120.

[62] K. Hong, S. Lee, Y. Yeon, and K. Jung, “Flexural response of reinforced concrete beams strengthened with near-surface-mounted Fe-based shape-memory alloy strips,” *Int. J. Concr. Struct. Mater.*, vol. 12, no. 1, pp. 1–13, 2018.

[63] H. Rojob and R. El-Hacha, “Fatigue performance of RC beams strengthened with self-prestressed iron-based shape memory alloys,” *Eng. Struct.*, vol. 168, pp. 35–43, 2018.

[64] S. Pan, M. Hu, X. Zhang, H. Hui, and S. Wang, “A new near-surface-mounted anchorage system of shape memory alloys for local strengthening,” *Smart Mater. Struct.*, vol. 28, no. 2, p. 25016, 2018.

[65] J. Michels, M. Shahverdi, C. Czaderski, and R. El-Hacha, “Mechanical Performance of Iron-Based Shape-Memory Alloy Ribbed Bars for Concrete Prestressing.,” *ACI Mater. J.*, vol. 115, no. 6, 2018.

[66] E. Hosseini, E. Ghafoori, C. Leinenbach, M. Motavalli, and S. R. Holdsworth, “Stress recovery and cyclic behaviour of an Fe-Mn-Si shape memory alloy after multiple thermal activation,” *Smart Mater. Struct.*, vol. 27, no. 2, p. 025009, Jan. 2018, doi: 10.1088/1361-665X/aaa2c9.

[67] E. Ghafoori, E. Hosseini, C. Leinenbach, J. Michels, and M. Motavalli, “Fatigue behavior of a Fe-Mn-Si shape memory alloy used for prestressed strengthening,” *Mater. Des.*, vol. 133, pp. 349–362, Nov. 2017, doi: 10.1016/j.matdes.2017.07.055.

[68] D. I. H. Rosa, A. Hartloper, A. de Castro e Sousa, D. G. Lignos, M. Motavalli, and E. Ghafoori, "Experimental behavior of iron-based shape memory alloys under cyclic loading histories," *Constr. Build. Mater.*, vol. 272, p. 121712, 2021, doi: 10.1016/j.conbuildmat.2020.121712.

[69] S. Raza, J. Michels, and M. Shahverdi, "Uniaxial behavior of pre-stressed iron-based shape memory alloy rebars under cyclic loading reversals," *Constr. Build. Mater.*, vol. 326, no. April, p. 126900, 2022, doi: 10.1016/j.conbuildmat.2022.126900.

[70] D. S. Simulia, "Abaqus 6.12 documentation," *Provid. Rhode Island, US*, vol. 261, 2012.

[71] J. B. Mander, M. J. N. Priestley, R. Park, and others, "Theoretical stress-strain model for confined concrete," *J. Struct. Eng.*, vol. 114, no. 8, pp. 1804–1826, 1988.

[72] H. Cornelissen, D. Hordijk, and H. Reinhardt, "Experimental determination of crack softening characteristics of normalweight and lightweight," *Heron*, vol. 31, no. 2, pp. 45–46, 1986.

[73] *CEB-FIP MODEL CODE 1990*. Thomas Telford Publishing, 1993. doi: 10.1680/ceb-fipmc1990.35430.

[74] V. Birtel and P. Mark, "Parameterised finite element modelling of RC beam shear failure," in *ABAQUS users' conference*, 2006, vol. 14.

[75] M. Pavlović, Z. Marković, M. Veljković, and D. Bucrossed D Signevac, "Bolted shear connectors vs. headed studs behaviour in push-out tests," *J. Constr. Steel Res.*, vol. 88, pp. 134–149, Sep. 2013, doi: 10.1016/J.JCSR.2013.05.003.

[76] J. L. Chaboche, "Time-independent constitutive theories for cyclic plasticity," *Int. J. Plast.*, vol. 2, no. 2, pp. 149–188, 1986, doi: https://doi.org/10.1016/0749-6419(86)90010-0.

[77] C. Fang, W. Wang, Y. Ji, and M. C. H. Yam, "Superior low-cycle fatigue performance of iron-based SMA for seismic damping application," *J. Constr. Steel Res.*, vol. 184, p. 106817, Sep. 2021, doi: 10.1016/j.jcsr.2021.106817.

[78] H. Dawood, M. ElGawady, and J. Hewes, "Behavior of Segmental Precast Posttensioned Bridge Piers under Lateral Loads," *J. Bridg. Eng.*, vol. 17, no. 5, pp. 735–746, Sep. 2012, doi: 10.1061/(asce)be.1943-5592.0000252.

[79] M. J. N. Priestley, F. Seible, and G. M. Calvi, *Seismic design and retrofit of bridges*. John Wiley \& Sons, 1996.

[80] J. Wang and Z. Wang, "Cyclic loading test of self-centering precast segmental unbonded posttensioned UHPFRC bridge columns," *Bull. Earthq. Eng.*, vol. 16, no. 11, pp. 5227–5255, 2018, doi: 10.1007/s10518-018-0331-y.

[81] Y.-C. Ou, "Precast segmental post-tensioned concrete bridge columns for seismic regions," State University of New York at Buffalo, 2007.

[82] J. M. Wacker, D. G. Hieber, J. F. Stanton, and M. O. Eberhard, "Design of precast concrete piers for rapid bridge construction in seismic regions," *Res. Rep*, 2005, Accessed: Jan. 05, 2023. [Online]. Available: https://www.wsdot.wa.gov/research/reports/fullreports/611.1.pdf

[83] J. B. Pang, J. F. Stanton, and M. O. Eberhard, "A precast concrete bridge bent designed to re-center after an earthquake," *Washingt. State Dep. Transp.*, 2008, Accessed: Jan. 05, 2023. [Online]. Available: http://www.wsdot.gov/research/reports/fullreports/684.3.pdf